Structure and deformation of the northern Canadian Cordillera: Insights from Rayleigh wave tomography

Submitted by: Morgan McLellan

Thesis presented to the Faculty of Graduate and Postdoctoral Studies in partial fulfilment of the requirements for the degree of Master of Science in Earth Sciences

Department of Earth and Environmental Sciences
Faculty of Science
University of Ottawa

Supervisor:
Dr. Pascal Audet (Department of Earth and Environmental Sciences)

Table of Contents

Abstract

We determine the crustal and upper mantle structure within the northern Canadian Cordillera using two complementary Rayleigh wave analysis techniques: ambient noise and teleseismic two-station interferometry. These methods are used to measure Rayleigh waves propagating between all available pairs of seismic stations in northwestern Canada, which are processed to obtain phase velocity dispersion curves. These curves provide information on the inter-station, path-averaged phase velocity as a function of frequency (or period). These inter-station phase velocities are then inverted to produce phase velocity maps. Phase velocity maps for periods between 8 and 80 s show to first-order high velocities within the Shield and low velocities within the Cordillera, supporting the thermal isostasy model for the region. Smaller scale features are observed throughout the Cordillera with high velocities west of the Tintina Fault reflecting the mafic composition of the accreted terranes of the Intermontane belt, and low velocities east of the Tintina fault reflecting the sedimentary rocks of the Selwyn Basin. High velocities extending west past the Cordilleran Deformation Front provide evidence for the existence of regions within the eastern Cordillera underlain by cool cratonic lithosphere. Anisotropy within the upper crust and mantle shows fast-axis orientations in line with the major faults within the region, providing evidence for a shear-zone that extends to lithospheric mantle depths. Lower crustal anisotropy shows an increase in heterogeneity of fast-axis orientations, which provides limited support for the existence of a weak shear zone and detachment within the lower crust. Results of a 1D inversion show approximate Moho depths of 35 km for the region west of the Tintina Fault, 36 km for the Mackenzie Mountains region, and 37 km for the shield. Reduced lower crust velocities observed throughout the Cordillera, provide support for the existence of a weak lower crustal layer.

Acknowledgments

I express my warm thanks to my supervisor Dr. Pascal Audet for his support, guidance, funding, and the opportunity to complete such a wonderful project. I would also like to thank Dr. Andrew Schaeffer, for without all of his hard work and dedication, this project would not have been possible. I would like to thank Stephen Mosher and Phillip Dales for their various suggestions throughout my project as well as providing technical support when needed.

I give a special thanks to my friends, for their help and encouragement over the past few years, for lending their support and help when necessary. I am eternally grateful to my parents for motivating me, my sister Gillian McLellan for her support, and to my boyfriend Anthony Lapp for his continued support and patience.

List of figures

1. Introduction

The northern Canadian Cordillera is a high elevation, low relief orogenic belt located in northwestern Canada that is part of the larger American Cordillera, which runs along the western portion of North and South America. The northern Cordillera extends from the BC-Yukon border in the south to the Beaufort Sea and eastern Alaska in the north and west, and its eastern extension abuts the Canadian Shield along the Cordilleran Deformation Front (Figure 1.1).

a b

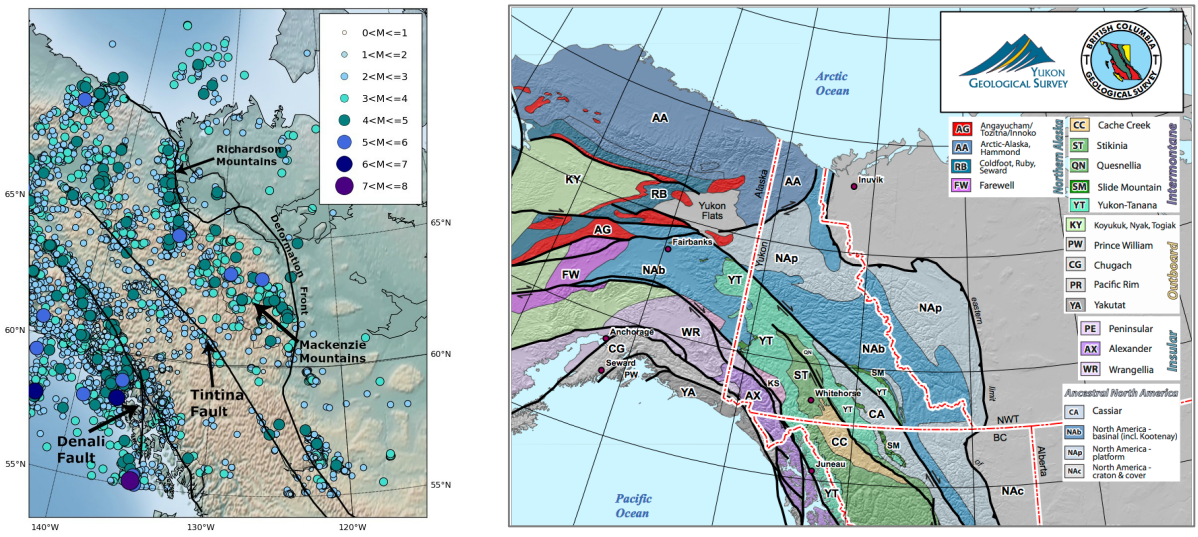

Figure 1.1: Map of (a) seismicity and (b) tectonic boundaries and provinces (terranes) in northwestern Canada and Alaska. Modified from Nelson & Colpron (2007).

It is one of the most seismically active regions in Canada, however the source of neotectonic deformation remains unclear. The deformation occurring within the Cordillera, most notably in the Mackenzie and Richardson Mountains, is believed to be a result of the collision of the Yakutat block onto the North American continental plate (e.g. Mazzotti & Hyndman, 2002; Hyndman *et al.,* 2005). Due to the great distance (600-800 km) between the collision zone and deformation front, rheological models have been developed to explain the

mechanisms in which strain transfer occurs over these long distances (e.g. Mazzotti & Hyndman, 2002). Knowledge of lithospheric structure is essential in providing further constraints on the processes that may explain the tectonic activity and strain transfer occurring throughout this region. Unfortunately, crustal structure beneath the northern Cordillera is poorly constrained due to the historically sparse distribution of seismograph stations in the area. Following the installation of new seismic networks in southern Yukon, western Northwest Territories and northern British Columbia as well as the progressive installation of stations in eastern Alaska and western Yukon from the Transportable Array of USArray, a high-resolution seismic investigation of the northern Canadian Cordillera is now possible.

In this thesis we attempt to further the understanding of Cordilleran structure and deformation through the completion of a high-resolution seismic tomography study of northwestern Canada using constraints from the analysis of surface-wave dispersion. In particular, we determine the vertically polarized (Rayleigh) wave phase velocity structure beneath the Cordillera between every possible pair of seismic stations using both ambient noise cross-correlation and teleseismic two-station interferometry. From these data we compute phase velocity maps, which provide insight on crust and mantle structure as well as deformation associated with major fault systems within the crust and with flow in the underlying mantle from seismic anisotropy.

1.1 Tectonic history of Northwestern Canada

Northwestern Canada has a tectonic history spanning billions of years, extending back to the Precambrian formation of the North American cratonic core (Hoffman, 1988). The amalgamation of former Archean microcontinents, whose collisional events are preserved in the Proterozoic belts of the region (e.g. the Trans-Hudson Orogen and Wopmay Orogen),

resulted in the formation of Laurentia, the core of the North American craton (Hoffman, 1988). Further accretionary events (e.g. Hoffman, 1988; Hildebrand *et al.*, 1987) docked the remaining pieces of the North American craton, which has remained mostly stable to this day. The tectonic history of the northern Canadian Cordillera, summarized by Monger & Price (2002) and Nelson *et al.* (2013), began approximately 750 million years ago when extensional forces associated with the break-up of the supercontinent Rodinia led to rifting within Laurentia and consequentially the formation of an ocean basin, which is the ancestor to the modern Pacific Ocean basin. In the Middle Devonian (~390 Ma) a convergent margin generated magmatic arcs offshore from the North American continental plate. Through continued subduction of the intervening sea, the continental margin eventually converged with the offshore oceanic arc, resulting in the accretion of these arcs to the continental plate, and beginning the formation of the Cordillera.

The Cordillera itself consists of a variety of accreted terranes, which have been mobilized across the fault systems, as well as the ancient rock from the cratonic core associated with the formation of Laurentia. The assemblage of these terranes can be subdivided into 5 categories as described by Nelson & Colpron (2007): 1) Ancestral North America (Laurentia), 2) Intermontane terranes associated with the ancient oceanic plate that existed off the west coast of North America in the Early Jurassic, 3) Insular and Farewell terranes, 4) Arctic Alaska, and 5) Younger (Mesozoic) accretionary terranes (Figure 1.1b).

The Selwyn Basin is located east of the Tintina Fault, and is comprised of thick Cambrian sedimentary sequences associated with the basinal and platformal rocks of the Ancestral North American margin (Hayward, 2015). West of the Tintina Fault is the Intermontane belt that consists of terranes accreted during the early Jurassic (Johnston *et al*., 1996) including the Cache Creek, Stikine, Quesnel, and Yukon-Tanana terranes, which have

subsequently been displaced northwestward along the Tintina fault. West of the Denali Fault are the Insular and Farewell Terranes. Unlike those of the Intermontane belt, the formation of these terranes is not associated with the western margin of North America but originated within the Arctic between Laurentia and Siberia (Nelson & Colpron, 2007). Furthest west are the Mesozoic to Paleogene accretionary terranes that include the Chugach, Pacific Rim, and Yakutat terranes, mainly comprised of trench sediments (Nelson & Colpron, 2007).

1.2 Current Seismicity in Northwestern Canada

The Yakutat Block is a continental-oceanic terrane that has been colliding with the North American continental plate since the Miocene (Mazzoti & Hyndman, 2002; Hyndman *et al.*, 2005). The Yakutat collision is responsible for the uplift of the Saint Elias and Chugach mountains along the western coast of the continent, a site of intense seismicity (Figure 1.1a). Furthermore, it is also believed to be responsible for the deformation occurring further east within the Mackenzie and Richardson Mountains (Mazzotti & Hyndman, 2002).

The distribution of seismicity in a given region is the most important indicator of ongoing tectonic deformation. The Queen-Charlotte-Fairweather fault system is the transform boundary that separates the North American continental plate and the oceanic Pacific plate. This fault accommodates most of the deformation resulting from the relative motion between the Pacific and North American plates and has produced earthquakes with magnitudes between 7.0 and 8.2 in 1927, 1949, 1958, 1972, and most notably the recent Haida Gwaii and Craig earthquakes that occurred in 2012 and 2013, respectively (e.g., Nishenko & Jacob, 1990; Doser & Lomas, 2000; Leonard *et al.*, 2008). As a result of the Yakutat-North America collision, there is an intense concentration of seismic activity in the region surrounding the collision zone, which includes the Chugach and St. Elias Mountains as well as the central

Alaskan Range further inland (Leonard *et al.*, 2007). A total of eight earthquakes of magnitude M > 7 have occurred in this region since 1899 (Cassidy *et al.*, 2005). Further east, the seismic activity is mainly concentrated along the Denali Fault, a right-lateral strike-slip fault. The rate of seismicity along this fault is an order of magnitude lower than that observed in the coastal regions (Cassidy *et al.*, 2005). The central portion of the northern Canadian Cordillera sees very little seismic activity with a minimal amount of earthquakes occurring along the Tintina Fault. Earthquakes of M ~ 4.5 are observed in this region, which suggests some activity along the right lateral strike-slip fault (Mazzotti & Hyndman, 2002). Further east the earthquake activity is distributed between two areas, one of which is located within the Mackenzie Mountains. This region consists of a fold and thrust belt that formed as a result of east-west compression (Hyndman *et al.*, 2005). Earthquakes of up to M ~ 7 have been observed within the Mackenzie mountains, which is remarkably high as there is no clear source of tectonic force that occurs in this region. The Richardson Mountains, located further north, exhibit a right lateral strike-slip component (Cassidy *et al.*, 2005) and has produced earthquakes of up to M ~ 6.5 along the north-south fault system (Mazzotti & Hyndman, 2002).

1.3 The Orogenic Float Model

Previous studies of crustal thickness in the region indicate an average thickness of 30-35 km throughout the North American Cordillera (Clowes *et al.*, 1995; Perry *et al.,* 2002; Kao *et al.*, 2013). In contrast, thicknesses of 40-45 km are observed in the surrounding craton (Kao *et al.,* 2013; Hyndman & Currie, 2005). This result contradicts our previous understanding of Cordilleran elevation, which predicts, according to Airy isostasy, the existence of thick crustal roots to support such high elevation belts. To account for this contradiction, the orogenic float model (Figure 1.2) postulates that elevated temperatures within the upper mantle beneath the

Cordillera allow for thermal expansion, and that this expansion supports the cordilleran elevations (Mazzotti & Hyndman, 2002; Currie & Hyndman, 2006; Hyndman *et al.,* 2005).

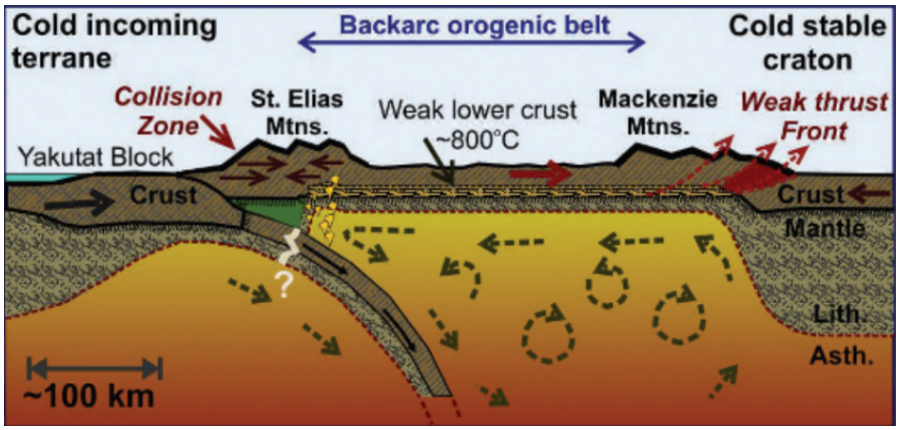

Figure 1.2: Model of weak, mobile, orogenic belt. From Hyndman *et al.* (2005).

Previous heat flow and elastic thickness studies confirm the variation in upper mantle temperatures throughout the region (e,g, Lewis *et al*., 2003; Audet *et al*., 2007). Lewis *et al*. (2003) estimated Moho temperatures based on constraints from heat flow-heat generation data, Moho-refracted P-wave (Pn) velocity, thermal isostasy, and lithosphere thickness. Based on these data, Moho temperatures of 800 ± 200 ºC to 950 ± 100 ºC were estimated in the Cordillera north of 59°N, and 850 ± 150 ºC in the Cordillera south of 59°N. Moho temperatures of 600 ± 200 ºC and 650 ± 150 ºC were estimated in the Wopmay Orogen, and temperatures between 350 ± 75 ºC and 500 ± 150 ºC were estimated in the Slave Craton. Cordilleran temperatures were estimated to be at least 150°C greater than any of the surrounding regions at all depths, and at least 300°C greater than temperatures observed in the craton. The Pn velocity data were collected from the SNORCLE transect and were used as proxy to constraint deep crustal temperatures. Upper mantle Pn velocities in the Slave craton

and foreland were shown to average at 8.0-8.2 km/s and decrease to 7.8-7.9 km/s in the Cordillera (Hyndman & Lewis, 1999; Lewis *et al.*, 2003). The difference in velocity was interpreted as being the result of large differences in Moho temperatures between the different regions. The seismic results also show uniformly thin crust (32-35 km) from the Slave craton to the western Cordillera despite a 1-2 km difference in surface elevation (Lewis *et al*., 2003). These results support the idea that elevated upper mantle temperatures are responsible for the high cordilleran elevation. An average temperature difference of ~250°C can be used to account for the 1600 m difference in elevation between the stable craton and the cordilleran region (Hyndman & Currie, 2011).

The increased temperatures observed in these back arc regions have further tectonic implications. The heat flow beneath the cordilleran crust is believed to create a detachment zone between a mechanically weak lower crust and a quasi-rigid upper crust (Mazzotti & Hyndman, 2002). This model proposes that motion associated with the Yakutat-North American collision is transferred to the upper crust and transmitted over 800 km inland as this rigid block is thrust over the leading edge of the craton (Mazzotti & Hyndman, 2002). The large displacement and strain developed within the crust by the proposed detachment zone are likely to leave an imprint in the form of seismic layering and anisotropy throughout the Cordillera, which can be constrained using seismic analysis techniques.

1.4 Previous Seismic Tomography Studies

Here we summarise the results of previous seismic studies that determined crustal and upper mantle structure beneath the Cordillera (Figure 1.3). A few continental-scale seismic velocity models obtained from surface-wave based measurements and waveform fitting approaches (e.g., Frederiksen *et al*., 2001; Bedle & Van der Lee, 2009; Yuan *et al.,* 2011;

Schaeffer & Lebedev, 2014) provide evidence that the cordilleran lithosphere has lower seismic velocities compared to those of the adjacent Canadian Shield, which is interpreted as increased upper mantle temperatures beneath the Cordillera. In a recent study, Kao *et al*. (2013) present the results of a Canada-wide tomography study using ambient noise data, which includes the Cordillera. The low number of stations within and across the Cordillera limits resolution, however the model is able to resolve a number of crust and uppermost mantle features. At shallow crustal depths, low velocity anomalies are observed within the Cordillera, in contrast to the Canadian Shield. This low velocity signature extends to the uppermost mantle. Moho depth is estimated throughout Canada with a relatively thick crust within the Shield, within the range of 35-41 km, whereas thin crust (~35 km) is associated with regions of active deformation, including the Cordillera. Moho topography within the Cordillera is seen to fluctuate between 25 and 38 km. We note that areas with a relatively shallow crust-mantle transition are not dominant and are typically associated with recent volcanic activity. Kao *et al*. (2013) suggest that Moho topography may be related to the mechanical strength or rigidity of the lithosphere and the pattern of mantle flow. Large mid-crust velocity gradients are also observed within the crust beneath the Cordillera. They ascribe this feature to the mid-crustal detachment zone predicted by the orogenic float model (Mazzotti & Hyndman, 2002).

A study conducted by Mercier *et al*. (2009) shows the results of upper mantle teleseismic body-wave tomography throughout western Canada. In these models, high velocities are observed within the eastern portion of the study area whereas low velocities are observed within the western portion. The transition between the low and high seismic velocity regions within the southern portion of the Cordillera is well defined at depths of 100 and 200 km and corresponds approximately with the Cordilleran Deformation Front. Further north, at latitudes of 55 degrees and above, the transition is less clear due to the high velocities observed west of

the Deformation Front (e.g., Schaeffer & Lebedev, 2014). These studies conclude that the main transition between cratonic and cordilleran lithosphere is aligned approximately with the Deformation Front, and that fast velocities observed west of the Tintina Fault may be associated with a seismically distinct Phanerozoic mantle lithosphere that has been displaced along the strike-slip boundary.

Refraction and reflection results produced using the SNORCLE transect (Snyder *et al*., 2002; Cook *et al*., 2004; Snyder *et al*., 2009) as well as a previous regional surface-wave tomography study (Dalton *et al*., 2011) provide evidence for the existence of continuous metasedimentary strata found throughout the Cordilleran crust. Reflection profiles show wedge shaped strata that are prominently reflective in comparison with the overlying crust and underlying mantle (Snyder *et al*., 2002). This wedge is found to begin at a hinge line east of the Cordillera and continues west, tapering beneath the accreted terranes. Dalton *et al*. (2011) attribute low velocities at 15 km depth to these metasedimentary rocks, as the eastern edge of the low velocity region correlates with the hinge line associated with the beginning of the wedge shaped strata. In this model, accreted terranes located in the eastern portions of the Cordillera are actually thin slices that have been thrust upon the strata. This implies that the western extent of the North American continent has remained stable since the Proterozoic.

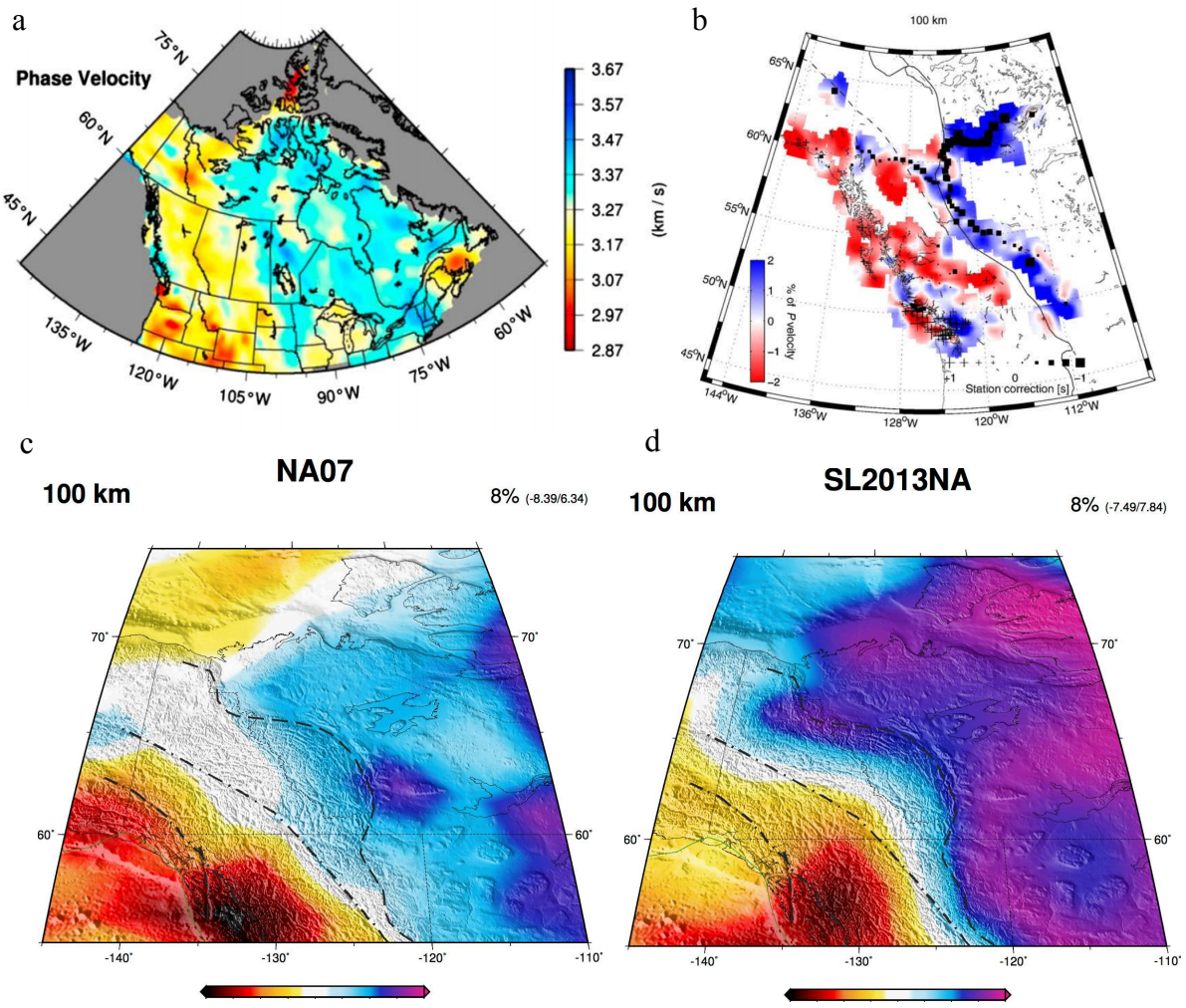

Figure 1.3: Previous phase velocity tomography (a) at 10 s period from Kao *et al.* (2013) and previous mantle tomography models (b) body wave tomography of Mercier *et al.* (2009) (c) surface-wave based tomography of Bedle & van der Lee (2009) and (d) multimode waveform inversion tomography from Schaeffer & Lebedev (2014).

In studies of seismic anisotropy (e.g. Courtier *et al*., 2010; Dalton & Gaherty, 2013; Audet *et al*., 2016) it is found that depths spanning the middle crust to upper mantle are seismically anisotropic throughout northwestern Canada. Shear-wave splitting data (Courtier *et al.,* 2010) resolve a change in the orientation of the fast axis from the craton into the Cordillera. Within the Cordillera, fast axes are roughly subparallel to the front range. This

suggests that the fabric is lithospheric in origin due to the abrupt transition and the strong correlation with surface tectonics. In a more recent study that incorporates additional stations through the northern Cordillera, Audet *et al.,* (2016) find that the majority of seismic anisotropy beneath the northern Canadian Cordillera is related to fossilized fabric associated with upper mantle shear zones rather than reflecting coherent sub-lithospheric mantle flow as predicted by the orogenic float model (Mazzotti & Hyndman, 2002).

2. Data and Methods

We determine the shear wave structure of the northern Canadian Cordillera and surrounding regions using phase velocity maps derived from fundamental-mode Rayleigh wave observations based on the vertical component broadband seismograph stations located in northwestern Canada and eastern Alaska. We used 69 stations (Figure 2.1) belonging to various networks including the Canadian National Seismograph Network (CNSN; CN), the US Array Transportable Array (TA), the Portable Observatories for Lithospheric Analysis and Research Investigating Seismicity (POLARIS; PO) network, the United States National Seismic Network (US), the Alaska Regional Network (AK), the Canadian Northwest Experiment network (CANOE; XN), and the Yukon-Northwest Seismic Network (YNSN; NY).

Data sources vary depending on the station and network. For stations belonging to the TA, US, AK, XN, and NY networks, vertical component seismograms were retrieved from the Incorporated Research Institutions for Seismology (IRIS) Data Management Center. For those stations belonging to the CN and PO networks, vertical component seismograms were retrieved from the Geological Survey of Canada.

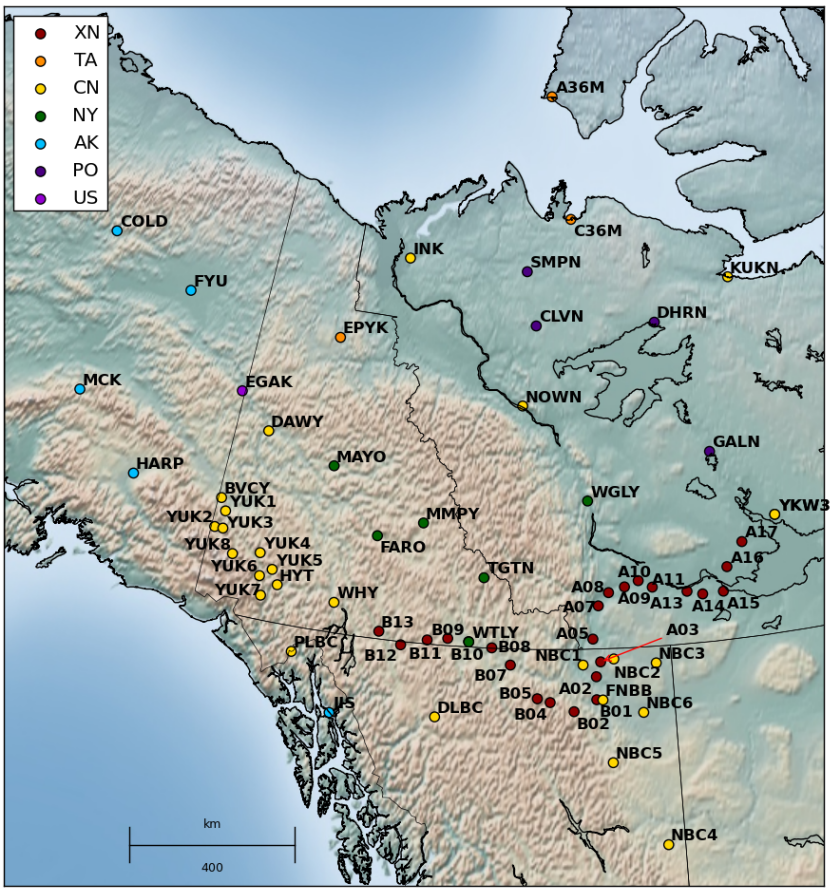

Figure 2.1: Map showing location of broadband seismic stations used in this study.

Fundamental-mode Rayleigh wave dispersion measurements were extracted between pairs of stations using two different and complementary methods: ambient seismic noise cross-correlation and teleseismic two-station interferometry. In both cases, the dispersion measurements—the variation in surface wave propagation speed as a function of period or frequency—provide constraints on the Earth structure between the station pairs. Ambient seismic noise measurements involve the cross-correlation and stacking of the simultaneously occurring noise traces at pairs of stations. This results in the production of empirical Green's functions, which represent virtual surface waves that would be observed if one station was the source and the other the receiver (Lobkis & Weaver, 2001; Campillo & Paul, 2003; Shapiro

& Campillo, 2004; Shapiro *et al*., 2005). Such ambient noise measurements generate signals with a dominant period range of 5-30 s, in comparison with a period range of 25-200 s for teleseismic earthquake signals. In the case of teleseismic two-station interferometry, rather than noise, signals from earthquake waves propagating along the great circle path that joins two station are cross-correlated, resulting in the estimation of surface waves travelling between the two stations (e.g. Meier *et al*., 2004; Darbyshire & Eaton, 2010). This technique utilizes the signals from teleseismic earthquakes dominantly at lower frequencies than ambient noise. Furthermore, the frequency band widens with increasing earthquake magnitude. Due to these differing frequency bands, the results obtained from ambient noise measurements and teleseismic two-station interferometry are highly complementary; together they can be used to resolve the Earth's structure across a greater depth range.

2.1 Ambient Noise Cross-correlation

The processing of ambient noise data can be summarized into 2 main steps as outlined by Bensen *et al.* (2007). The two steps are: 1) single station data preparation, and 2) cross-correlation and temporal stacking. Firstly, vertical component data were collected as day-long traces from all stations in the northern Canadian Cordillera and surrounding regions. The amount of data collected depended on the data availability for the specific station. Using longer time series is ideal as it improves the signal to noise ratio, but these effects become negligible after 3 years, and as such was the maximum length of data collected (Kao *et al*., 2013). To prepare the traces for cross-correlation, the data were de-meaned and de-trended to avoid edge effects, and resampled at a rate of 1 Hz to ensure a consistent sampling rate for all stations as well as increasing computational efficiency. The instrument response was then deconvolved and the signal was converted to displacement. Next, the data underwent

'temporal normalization', which is the procedure for reducing the effects of earthquake signals, instrument irregularities, and non-stationary noise sources from the ambient noise data (Bensen *et al*., 2007). These effects were removed using a technique known as 'one-bit normalization.' Here only the sign of the amplitude is retained; all positive valued amplitudes are replaced with 1 and all negative valued amplitudes with -1. This method is commonly used, has been demonstrated to be robust, and was employed in the earliest studies using ambient noise (Campillo & Paul, 2003; Shapiro & Campillo, 2004; Shapiro *et al*., 2005).

Finally, the data were 'spectrally whitened' to account for the fact that ambient noise data does not have a flat amplitude spectrum in the frequency domain. Spectral whitening acts to broaden the band of the ambient noise signal in cross-correlations and remove unwanted peaks found in the frequency domain that dominate the spectra. Traces were spectrally whitened between 0.005 and 1 Hz (200 to 1 s period). Hour long noise traces, for a given station, were cross-correlated with the corresponding time-window trace for all available stations. Station availability was limited based on the deployment times of a given seismograph. The resulting individual cross-correlations for each station pair were stacked over a period of time corresponding to the data availability. The resulting traces are signals with both a positive lag component, known as the "causal" signal, and a negative lag component, known as the "acausal" signal (Figure 2.2).

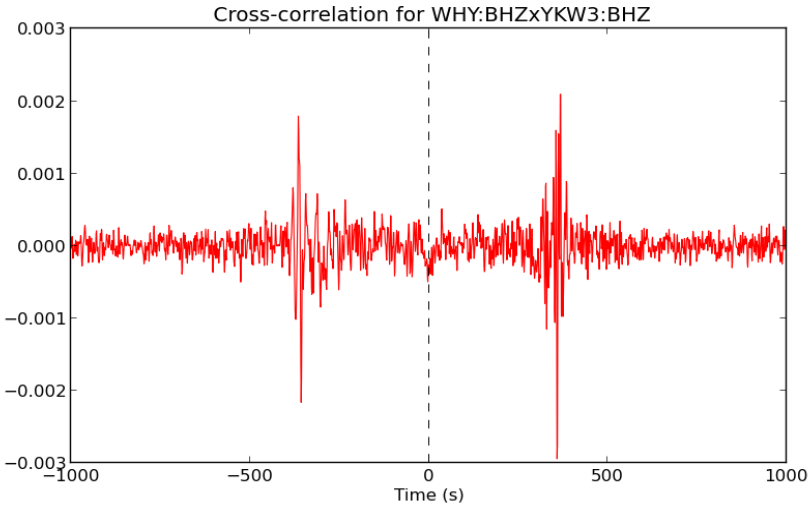

Figure 2.2: Cross-correlation for stations WHY and YKW3. The two peaks represent the "causal" and "acausal" signals, which are the resulting surface waves that would be produced if one station were the source and the other the receiver.

These represent the seismic waves travelling in both directions, from one station to the other and *vice versa* (Bensen *et al*., 2007). In ideal cases, in which noise distribution is homogeneous, the causal and acausal signals are nearly symmetric. However, this is rarely the case in practice due to the irregular distribution of noise sources, and is particularly relevant for the northern Cordillera due to the dominant noise source being the ocean in the west.

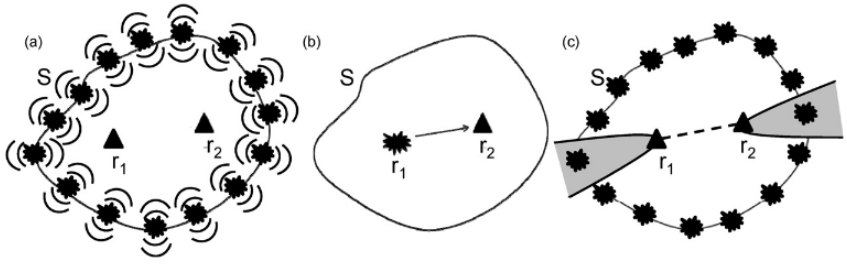

Figure 2.3: Illustration of ambient noise interferometry concept. (a) Two receivers surrounded by a homogenous distribution of seismic sources. (b) Interferometry turns one of the receivers into a virtual source (r1) where a seismogram is recorded at the second receiver (r2). (c) The seismogram recorded at r2 is constructed based on the seismic waves that travel on a direct path between the two receivers (grey region). From Nicholson *et al.* (2009).

To account for this effect, we construct a "symmetric" signal, computed as the average of the causal and acausal signals (Bensen *et al*., 2007); this trace represents the virtual surface wave that would be observed if one of the stations was the source and the other the receiver, given a quasi-symmetric noise distribution (Figure 2.3). Figure 2.4 shows the results of the symmetric cross-correlation of station EPYK with all other available stations.

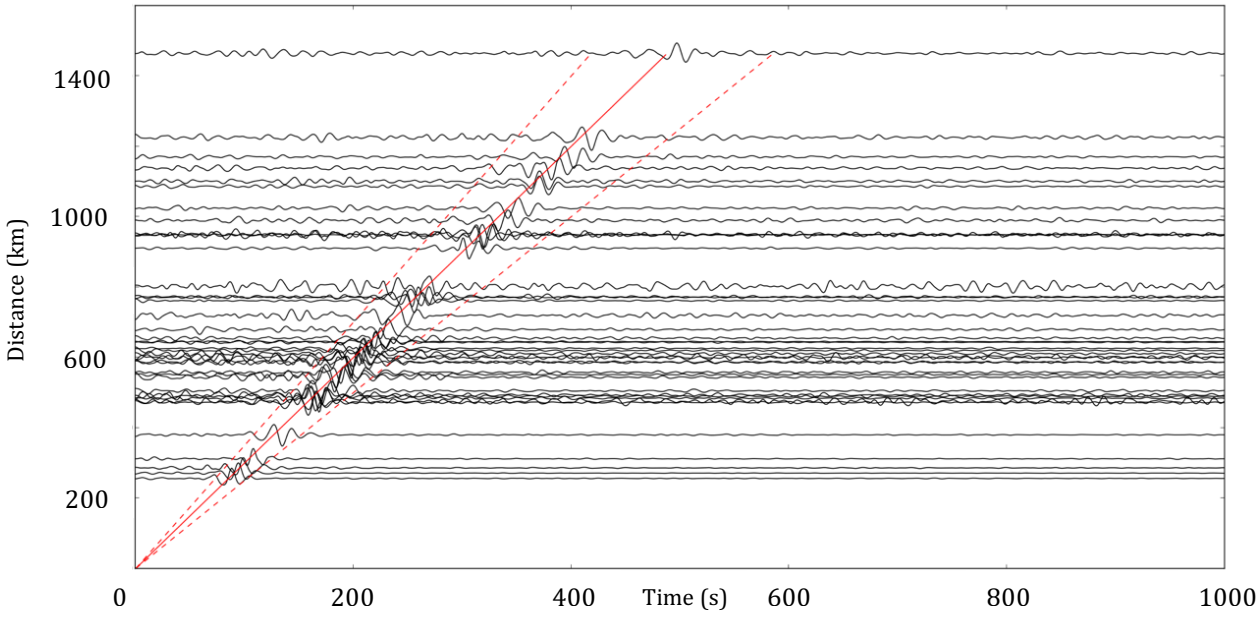

Figure 2.4: Cross-correlations produced between EPYK and all other available stations plotted based as a function of interstation distance. Mean, minimum and maximum expected surface wave velocities are represented by the red solid and dashed lines.

The same stations used in the ambient noise analysis were again used here. From these stations, vertical component seismograms recording teleseismic earthquakes were collected. We used minimum magnitude thresholds between 5.0 and 5.8 depending on the abundance of data available for each station pair. Decreasing the minimum magnitude increased the number of available events, allowing for additional data, however at the cost of noisier measurements. As a result, lower magnitude thresholds were only used at select stations with limited amounts of data. After the initial data collection, a selection criterion was applied to all of the listed

events; for each station pair, the epicenter of the teleseismic event must lie within ±5° of the inter-station great circle path. Including only the events that meet this criterion allows us to assume a direct travel path between the two stations in question (Darbyshire & Eaton, 2010). The selected waveforms were then processed prior to cross-correlation. The processing included resampling to 1 Hz, removal of the instrument response and conversion to displacement, as well as filtering using a low pass filter with a corner frequency of 0.5 Hz. Finally, we cross-correlated the event signal recorded at each station pair to produce a new seismogram from which we measure the surface wave dispersion for each earthquake that met the selection criterion.

2.3 Rayleigh Wave Phase Dispersion Measurements

We used surface-wave data from both the ambient noise and the teleseismic two-station approaches to estimate Rayleigh wave phase dispersion curves. Bensen *et al*. (2007) describes the process from which one can extract phase velocity curves from cross-correlated data. We use the time-domain analytic signal:

$$S_a(t) = s(t) + iH(t) \quad (1)$$

$$= A(t)e^{i\emptyset t} \quad (2)$$

and in the frequency domain as:

$$S_a(\omega) = S(\omega)(1 + sgn(\omega)) \ , \quad (3)$$

where $S_a(t)$ and $S_a(\omega)$ are the analytic signal in their respective domains, $s(t)$ and $s(\omega)$ are the original surface-wave signal, $H(t)$ is the Hilbert transform of $s(t)$, $A(t)$ is the amplitude, and $\phi(t)$ is the phase. To determine the frequency-time relationship, a series of Gaussian filters was applied to the analytic signal in the frequency domain:

$$S_a(\omega, \omega_0) = S_a(\omega) G(\omega - \omega_0) \quad (4)$$

with

$$G(\omega - \omega_0) = e^{(-\alpha(\omega-\omega_0)/\omega_0)\text{^}2} \quad , \quad (5)$$

where ω_0 represents the central frequency of the Gaussian filter $G(\omega)$, and α is a tunable parameter. The filtered analytic spectrum is transformed back into the time domain via inverse Fourier transform, which provides the instantaneous envelope and phase of the original signal based on the central frequency of the Gaussian filter. In other words, the frequency-time representation of the Rayleigh wave signal is produced, from which group and phase velocities can be measured from the envelope and phase of the 2-D plots, respectively. Since the distance between the two stations is known, the arrival time of the energy peak can be converted to velocity and the relationship between velocity and the frequency can be determined based on the central frequency of the Gaussian filters. Here we use only the phase velocity derived from the phase of the analytic signal, which is composed of a propagation term, an initial source phase, and a phase ambiguity term, $2n\pi$, where n is a whole number (Bensen *et al*., 2007). To compute the phase-velocity dispersion measurements we follow the procedure outlined in Meier *et al*. (2004), which uses the JWKB approximation formulation to help with unwrapping the phase ambiguity term.

After the creation of the phase dispersion curves we manually select the appropriate frequency bands by plotting each curve against the reference curve (AK135; Kennett *et al*, 1995) representing average Earth structure. The curve nearest to the reference curve is selected, allowing for easy visual disambiguation of the phase ambiguity. The reference curve also acts as an approximation that allows for the selection of the "good" parts of each calculated dispersion curve (i.e., curves that follow a similar dispersion path). The selection

window is shown in Figure 2.5. After selecting the curves for every event, an average curve for each station pair was produced. A second round of selection was done in which parts of the curves that did not follow the trend were removed, thus producing a smoother curve. Additional rounds of selection were done if required. The curves were then cut at high and low periods if they began to deviate unrealistically from the reference curve. This produced a final average dispersion curve representing the dispersive characteristics of the subsurface between each station pair. From the ensemble of original curves, we calculate the error associated with the curve, which is determined by the standard deviation.

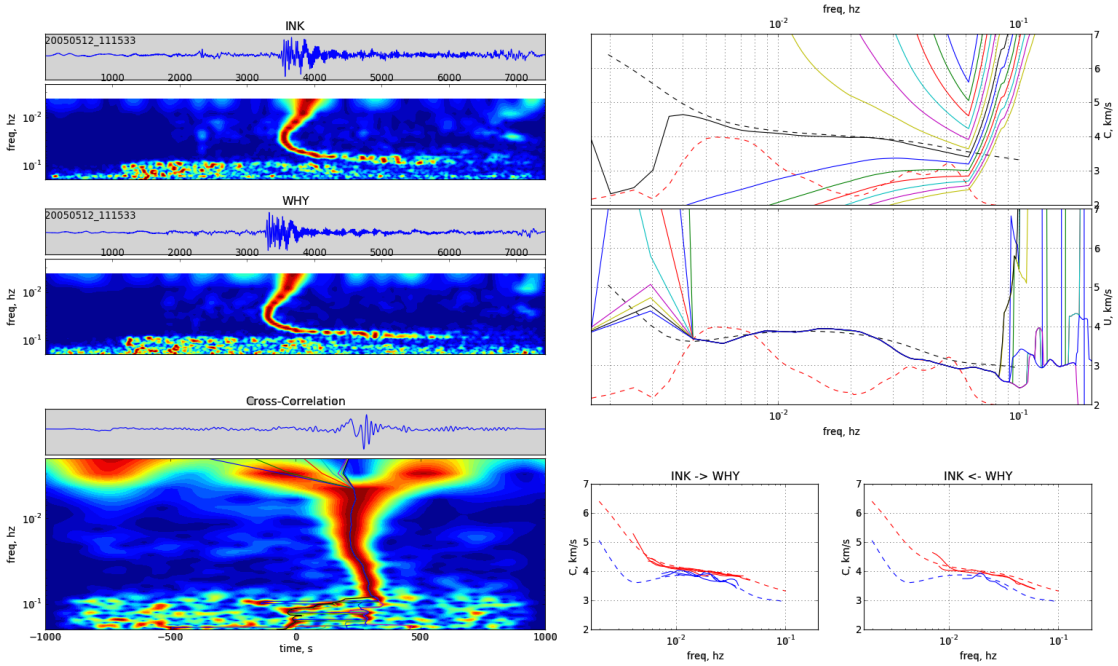

Figure 2.5: Example of interactive selection for an earthquake on 12 May 2005. Left panels: Seismogram and spectrogram for INK and WHY; bottom shows the cross-correlation time-series and accompanying spectrogram. Right panels: interactive phase (top) and group (middle) velocity selection windows. For phase velocity, the coloured curves represent various possible solutions given the 2nπ phase ambiguity; we identify and select only the smooth parts of that curve which lies reasonably close to the reference. Bottom right panels track the selected phase (red) and group (blue) curves for the given pair for events from each direction. Group velocity results are not presented in this study.

2.4 Combining Dispersion Curves

Ambient noise and teleseismic interferometry produce inter-station Rayleigh wave dispersion curves characterized by different bandwidths. Ambient noise data can be used to obtain robust dispersion curves at short periods (~5 to 30 s), whereas teleseismic earthquakes have a much wider bandwidth that extends to longer periods (20 to >200 s). The two methods therefore produce dispersion curves at overlapping periods (~20 to 30 s); however, these curves may slightly diverge in this period band. We investigate the consistency of the dispersion curves produced by the two approaches by plotting and inspecting the curves for two station pairs that are typical of our data set. Figure 2.6a shows the resulting ambient noise and teleseismic dispersion curves plotted against each other for stations COLD and KUKN. Here, the overlap between the two curves at periods between 25 s and 35 s is good and selecting between the two methods is not essential; the two curves can be safely averaged. More commonly observed is the divergence between the two curves at overlapping periods as shown for stations JIS and NBC1 in Figure 2.6b.

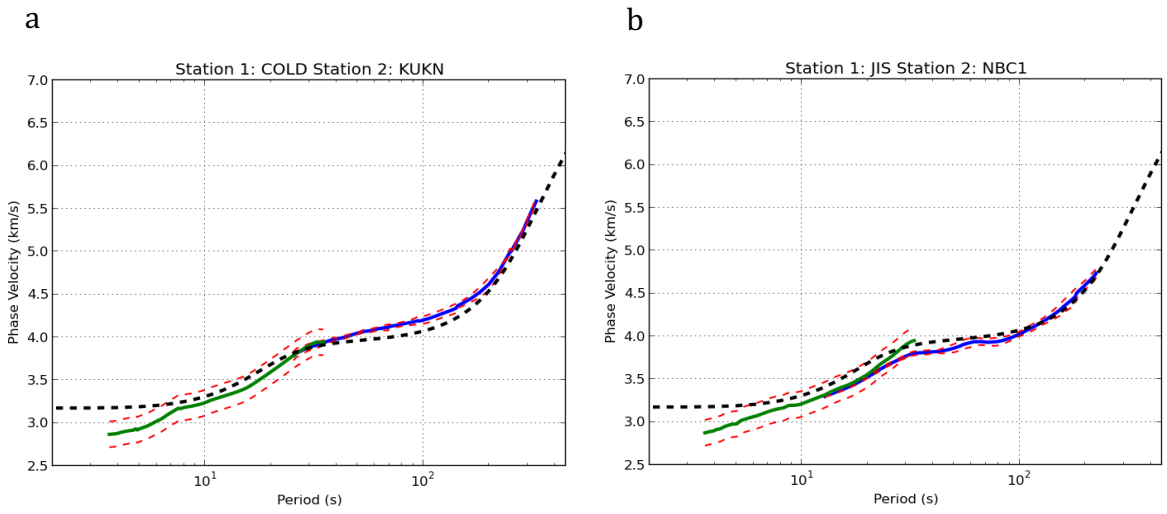

Figure 2.6: Ambient noise (green) and teleseismic two-station (blue) phase velocity curves for stations (a) COLD and KUKN and (b) JIS and NBC1. Error is represented by the dashed red line. The black dashed line is the reference curve from AK135.

Here, two ambient noise and teleseismic curves begin to overlap at approximately 13s and are nearly identical until approximately 20 s. At 20 s the ambient noise and teleseismic curve begin to deviate significantly from one another. Given the dominant sensitivity bands of ambient noise and teleseismic events, we select ambient noise data for periods up to 25 s and teleseismic data for periods 30 s and above in the construction of the phase velocity maps. The combined inversion of ambient noise and teleseismic interferometry is the subject of continued work.

2.5 Tomographic Inversion for Phase-Velocity Maps

The dispersion curves produced for each station pair were then inverted to produce azimuthally anisotropic phase-velocity maps. Here we follow a similar procedure to that outlined in Deschamps *et al*. (2008) and Darbyshire & Lebedev (2009). We construct phase velocity maps by solving the following equation at a discrete set of frequencies, ω:

$$\int \int K_i(\omega, \theta, \phi) \delta C(\omega, \theta, \phi) d\phi d\theta = \delta C_i(\omega), \quad (6)$$

where θ, ϕ represent the latitude and longitude coordinates of the given knot point within the study region, ω is the frequency, $\delta C_i(\omega)$ is the inter-station phase velocity anomaly at frequency ω for the ith station pair, $K_i(\omega, \theta, \phi)$ is the sensitivity kernel that maps the ith station pair's path to the knots on the grid, and $\delta C(\omega, \theta, \phi)$ is the model we are trying to solve for. For each frequency, we linearize the above equation solving for perturbations from a reference phase velocity; this reference is removed from each interstation phase velocity measurement, transforming the data to $\delta C_i(\omega)$ and solving for phase velocity perturbations from that same reference, $\delta C(\omega, \theta, \phi)$. The model we wish to solve for, the phase velocity anomaly at any given longitude (θ) and latitude (ϕ), is broken down as:

$$\delta C(\theta, \phi) = \delta C_{\text{iso}}(\theta, \phi) + \delta C_{2\psi}(\theta, \phi) + \delta C_{4\psi}(\theta, \phi) \quad (7)$$

where (δC_{iso}), ($\delta C_{2\psi}$), and ($\delta C_{4\psi}$) indicate the isotropic, 2ψ and 4ψ components, respectively. This can be further expanded, parameterizing the isotropic, 2ψ, and 4ψ components of the phase-velocity in terms of their sine and cosine terms (e.g. Smith & Dahlen, 1973):

$$\delta C(\omega) = \delta C_{\text{iso}}(\omega) + A_1(\omega)\cos(2\psi) + A_2(\omega)\sin(2\psi) + A_3(\omega)\cos(4\psi) + A_4(\omega)\sin(4\psi) \quad (8)$$

We build a system of linear equations for each period according to eq. 8 by mapping each of the interstation dispersion curves onto our model grid, and solve it using the LSQR method (Paige & Saunders, 1982), subject to lateral smoothing and norm damping to minimize the effects of errors in the data. We utilize a spherically-tessellated triangular grid (Wang & Dahlen, 1995). This method produces a grid with approximately equal inter-knot spacing, which is important for the application of smoothing and damping at higher latitudes (such as our study region) we select a target model-grid spacing of 75 km. We attempt to find the model vector, $\vec{m}$, by minimizing the following equation:

$$\left|\boldsymbol{A}\vec{m} - \vec{d}\right| + \alpha|\boldsymbol{I}\vec{m}| + \lambda|\boldsymbol{\Lambda}\vec{m}| + \gamma|\boldsymbol{\Gamma}\vec{m}| \quad (9)$$

where $\boldsymbol{A}$ is the kernel matrix, $\vec{d}$ is the data vector, $\vec{m}$ is the preferred model, $|\boldsymbol{A}\vec{m} - \vec{d}|$ is the misfit between the synthetic data predicted by the preferred model and the real data, α, λ and γ are the norm damping, lateral smoothing and gradient damping coefficients, $\boldsymbol{I}$ is the identity matrix, $\boldsymbol{\Lambda}$ is the lateral smoothing operator, and $\boldsymbol{\Gamma}$ is the lateral gradient operator. In this work we focus our attention dominantly on lateral smoothing and norm damping, and use a small coefficient value of γ (which has the largest effect at the model domain boundaries). Increasing the values of α and λ increases the relative importance of the damping and smoothing terms respectively, in the minimization. Setting the values of α and λ to 0 produces a model computed whereby only the model misfit contributes to the minimization. A range in

smoothing and damping parameters were then tested by inspecting the effects different coefficient values had on numerous inversion results. Over-smoothing (large λ) sufficiently reduces the effects of errors, but can result in lack of resolution, blurring the appearance of anomalies. Under-smoothing (small λ), on the other hand, does not remove the effects of noise and errors sufficiently, resulting in the appearance of false anomalies.

Selection of the ideal parameter values was accomplished through analysis of the trade-off between model misfit—the difference between the estimated model and the data—and model norm—which describes the size of the model. Here we plot (Figure 2.7) the model misfit against the model norm for different smoothing and damping parameters while keeping the other constant. This produced a trade-off curve where the optimal parameter is selected based on the point of maximum curvature, or in other words, where the model misfit and norm do not change much with changing damping or smoothing (Hansen, 1998).

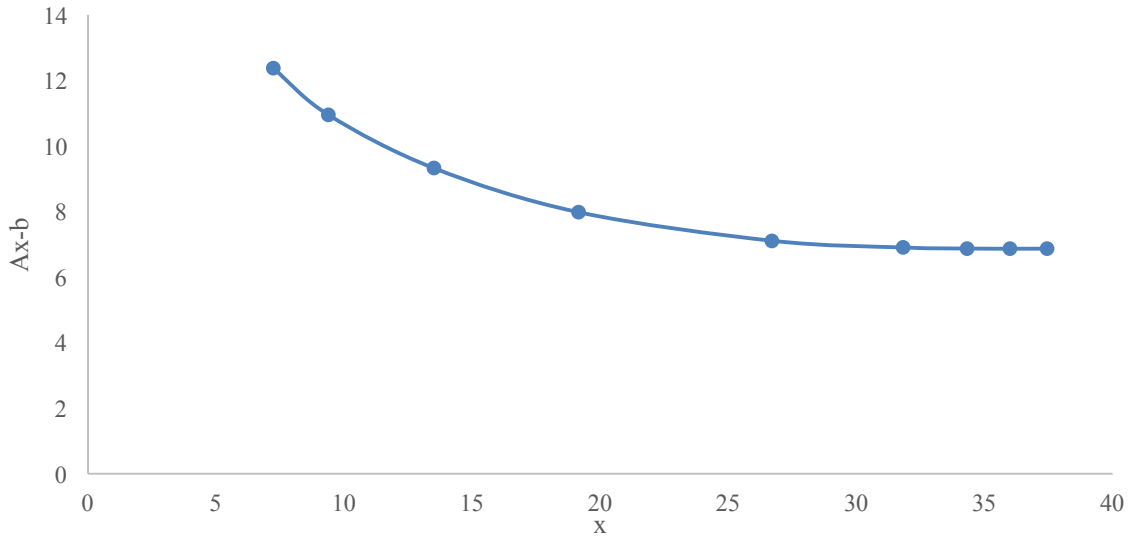

Figure 2.7: Example L-curve produced using a smoothing value of 0.15 while varying norm damping values. Area of curve with maximum curvature was selected as ideal norm damping value. Here the parameter "x" represents the model vector "m".

The ideal parameter selection was reinforced by our knowledge of the geology of the region and was based on the reasonable expectation of velocity anomalies and from previous work (e.g., Dalton *et al.*, 2011). These steps result in azimuthally anisotropic phase velocity maps for the selected periods.

Next we perform an analysis of data outliers to remove paths that least fit the selected model. We analyze the distribution of the normalized data-synthetic residual and remove any input data for which equations lie outside a selected threshold (see Schaeffer & Lebedev, 2013, for details on outlier analysis). We compared the results produced by removing 5%, 10%, 20%, and 25% of the input data with highest residuals. Increasing the percentage can lead to more reliable measurements and a lower remaining variance, but at the expense of path coverage. Based on optimizing the trade-off between path-coverage and synthetic-data misfit, we first removed 5% of the input data and selected curves that were kept for all periods. A second round of the outlier exclusion process was done where 10% of the data was removed to ensure a reasonable remaining variance.

2.6 Inversion for 1-D velocity profiles

As phase velocity is a depth-integrated quantity, on its own it does not provide directly interpretable constraints on the variation in seismic velocity as a function of depth. We therefore invert the Rayleigh wave dispersion curves to produce 1D shear velocity profiles, following the procedure outlined in Lebedev *et al*. (2008) and Agius & Lebedev (2013; 2014).

The inversion is solved using a Levenberg-Marquaardt gradient search (implemented in MatLab ®) where the model is fit by solving a fully nonlinear least squares problem. Synthetic phase-velocities are computed iteratively from the V_{sv} models using the MINEOS normal

mode code (Masters, http://geodynamics.org/cig/software/mineos). The inversion minimizes the misfit between the original and synthetic data, where the synthetic data is computed from an iteratively perturbed background model. Perturbations from the background model are controlled by basis functions which consist of boxcars in the crust and triangles in the mantle. The basis function defines the sensitivity of perturbations to isotropic velocities within each depth range. Discontinuities are parameterized using half triangles, such that the velocities above and below can be varied independently.

The inversion for shear-velocity models from surface wave dispersion measurements is highly non-unique (Lebedev *et al*., 2013). To obtain a final model, *a-priori* information about the crustal structure and approximate Moho depths are included in the background model, providing further constraints on the final profile. Included in the background model were three separate crustal layers whose thicknesses, and in turn the depth to the Moho, could be altered depending on the input data. Damping parameters were adjusted at various depths to control the degree of freedom given to the inversion in adjusting velocity structure; these values depend in part on the uncertainty of the input data and the expected relative sensitivity as a function of frequency.

When surface waves reach the Moho, there is an increase in velocity from the crust to the mantle. Since we do not know the exact Moho depth, nor the seismic velocities in the crust and mantle, there exists a trade off between the parameters for shear speeds and Moho depth due to the non-uniqueness of surface-wave sensitivities. Changes in Moho depth can therefore be compensated by either increasing or decreasing the seismic velocity above or below the Moho, produce very similar data misfits (Lebedev *et al*., 2013).

3. Results

3.1 Dispersion Curves

Figure 3.1 shows the complete set of curves observed for all station pairs, combining both ambient noise and teleseismic two-station results. There is an increase in variability in velocity at shorter periods due to the substantially greater heterogeneity in structure sampled at these crustal depths. Longer periods sample both deeper depths and a greater range in depth and will therefore represent more averaged structure, producing less variability in the curves.

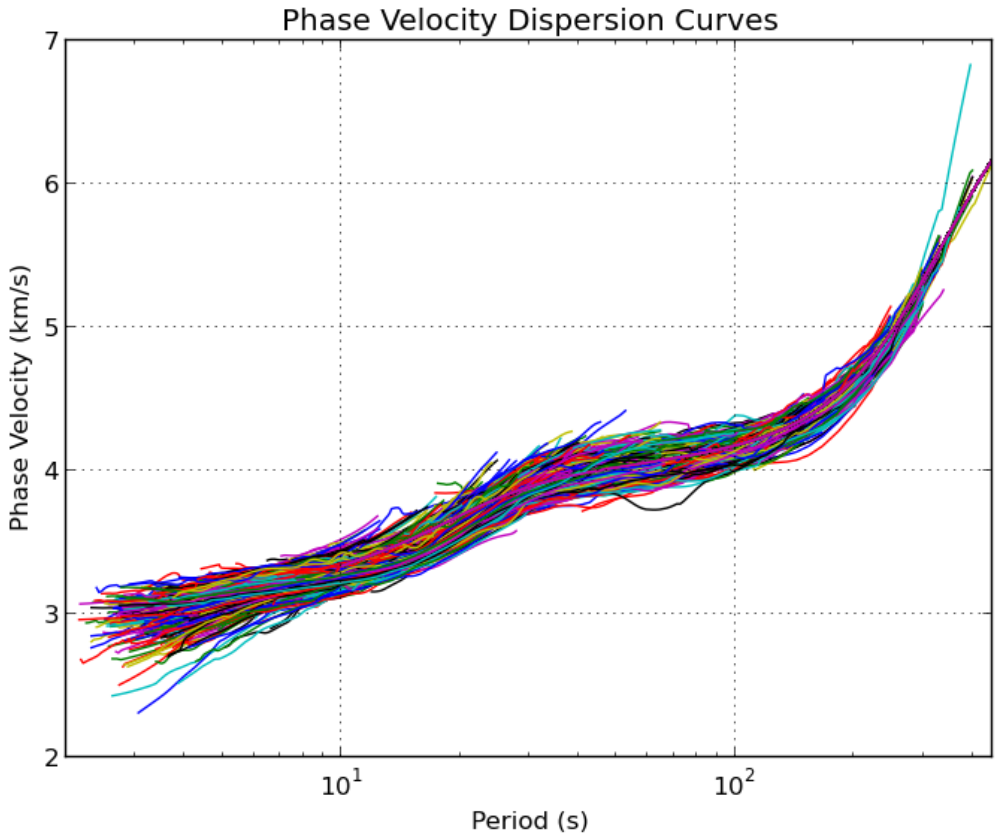

Figure 3.1: Ambient noise and teleseismic two station phase velocity dispersion curves plotted for every station pair.

From all these curves, we selected three separate regions and generated average curves

for each by selecting representative curves based on data quality (e.g. smoothness of the curve and level of agreement between ambient noise and teleseismic data for overlapping periods). We produced such average curves for the region west of the Tintina Fault (Group 1, green), within the Mackenzie Mountains (Group 2, blue), and east of the Deformation Front (Group 3, red).

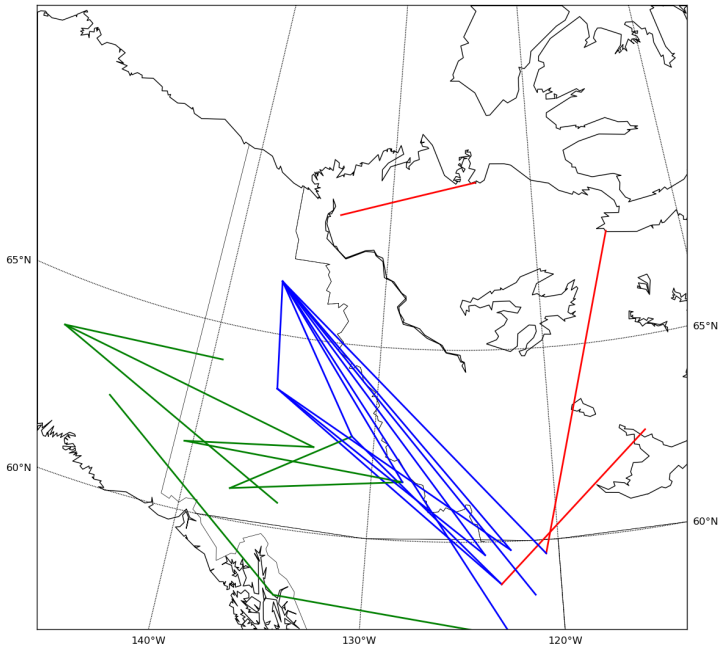

Figure 3.2: Interstation paths used to produce an average curve for each region. Green paths were used for Group 1, the region west of the Tintina fault; blue paths were used for Group 2, the Mackenzie Mountain region; and the red paths were used for Group 3, the region located within the shield.

Interstation paths for each station pair that were used to produce the average curve for each region are shown in Figure 3.2 and resulting average curves are shown in Figure 3.3. The average curve produced for the region west of the Tintina fault shows consistently low velocities (~0.2 km/s slower) in comparison with the AK135 reference model for all periods. This difference becomes increasingly smaller at 100 s until the curve closely follows the

reference curve at 200 s. The representative curve for the Mackenzie Mountains region also shows low velocities (~0.2 km/s slower) beginning at 6 s and continuing until 40 s where the curve begins to overlap with the reference curve. The dispersion curve does not deviate from the reference curve until it ends at approximately 300 s. For the dispersion curve representing the region east of the Deformation Front, the curve follows the reference curve until approximately 20 s where there is a shift to higher velocities (1-2 km/s). This continues until approximately 225 s where the curve begins to align itself with the reference curve once again.

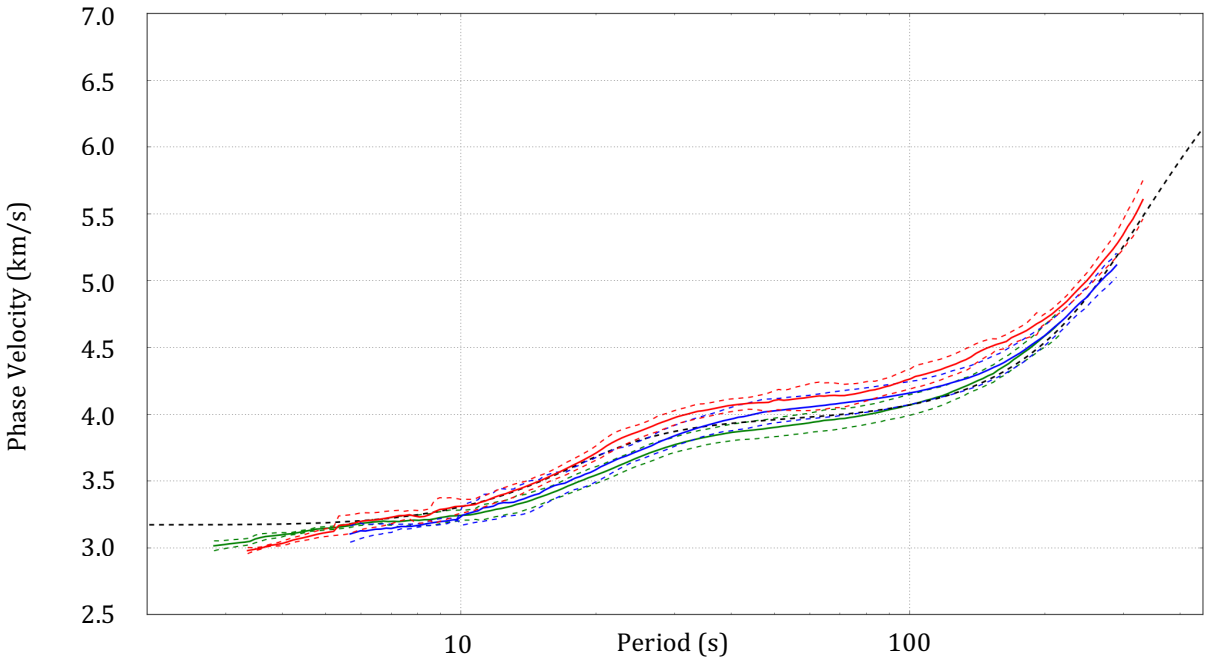

Figure 3.3: Average phase velocity curves for each region (Groups 1-3; Figure 3.2). The green curve represents the region west of the Tintina fault, the blue curve represents the Mackenzie Mountain region, and the red curve represents the region located within the shield. The AK135 reference model for average crustal and upper mantle velocity is represented by the black dashed curve.

3.2 Inter-Station Phase Velocities

The spatial variability in dispersion curves can be visualized on a map, where inter-

station paths at each period are color-coded according to the measured phase velocity. In Figure 3.4 we show inter-station phase velocity maps at periods of 8, 15, and 25 s obtained from ambient noise cross-correlation, and periods of 35, 60, and 80 s obtained using teleseismic earthquakes. In addition to displaying spatial patterns in phase velocities, the maps provide a visual appreciation of spatial resolution of the resulting phase velocity maps (next sections). In general, the maps obtained using ambient noise data show many more inter-station paths compared to those obtained from teleseismic earthquakes. This reflects the greater restrictions imposed by the teleseismic two-station method that requires earthquakes to be located within a small great circle path aligned with both stations.

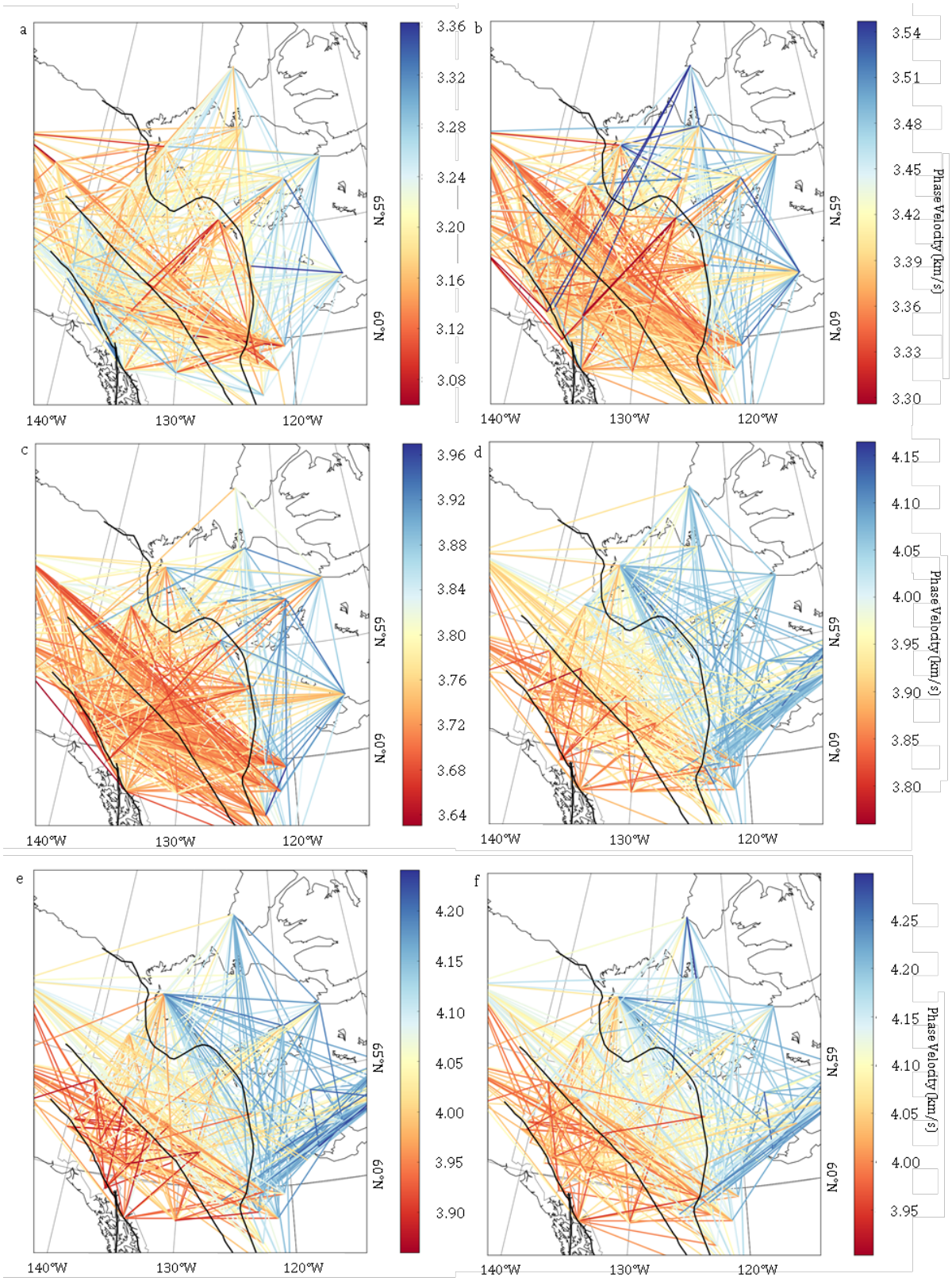
a
b
c
d
e
f
65°N
60°N
140°W
130°W
120°W
3.36
3.32
3.28
3.24
3.20
3.16
3.12
3.08
3.54
3.51
3.48
3.45
3.42
3.39
3.36
3.33
3.30
3.96
3.92
3.88
3.84
3.80
3.76
3.72
3.68
3.64
4.15
4.10
4.05
4.00
3.95
3.90
3.85
3.80
4.20
4.15
4.10
4.05
4.00
3.95
3.90
4.25
4.20
4.15
4.10
4.05
4.00
3.95
Phase Velocity (km/s)

Figure 3.4: Interstation phase velocity maps plotted at (a) 8, (b) 15, (c) 25, (d) 40, (e) 60, and (f) 80 s. Interstation paths are colour coded according to measured phase velocity. Major tectonic features are represented by the black lines where, from west to east, the location of the Denali Fault, Tintina Fault, and Deformation Front are represented.

The maps obtained for short periods (8, 15 and 25 s) display greater variability in phase velocities compared to those at longer periods (35, 60 and 80 s), reflecting more heterogeneous shallow (mostly crustal) compared to deeper (mostly mantle) structure. At most periods, inter-station paths that propagate across the Cordillera show low phase velocities while those in the Shield show relatively higher phase velocities. At 8 and 15 s, high phase velocities are also observed toward the western part of the Cordillera, with a transition located around the Tintina Fault. The lowest phase velocities at periods of 8, 15 and 25 s all occur within the eastern part of the Cordillera, and the transition between high and low phase velocities at the Cordilleran-Craton boundary becomes apparent at 15 s. At periods of 35, 60 and 80 s the patterns become more regular and show a gradient from the lowest phase velocities in the westernmost part of the Cordillera, increasing toward the Canadian Shield. Interestingly, the Cordillera-Craton boundary is not as sharp at that observed at a period of 15 s, and relatively high phase velocities more typical of the Canadian Shield appear to extend into the Cordillera.

These inter-station phase velocity curves are the input to the tomographic inversion. We now turn to resolution tests in order to investigate the level of detail that we can confidently interpret in the tomographic phase velocity maps.

3.3 Resolution Tests

Results of the checkerboard test for ambient noise and teleseismic data are shown in Figure 3.5. Here the synthetic input data is produced by constructing checkers approximately

300 km x 300 km (4 × 4 knots with a knot spacing of 75 km) alternating isotropic velocity anomalies of positive and negative 100 m/s, and 2Ψ anisotropy anomalies (2%) oriented at plus and minus 45°.

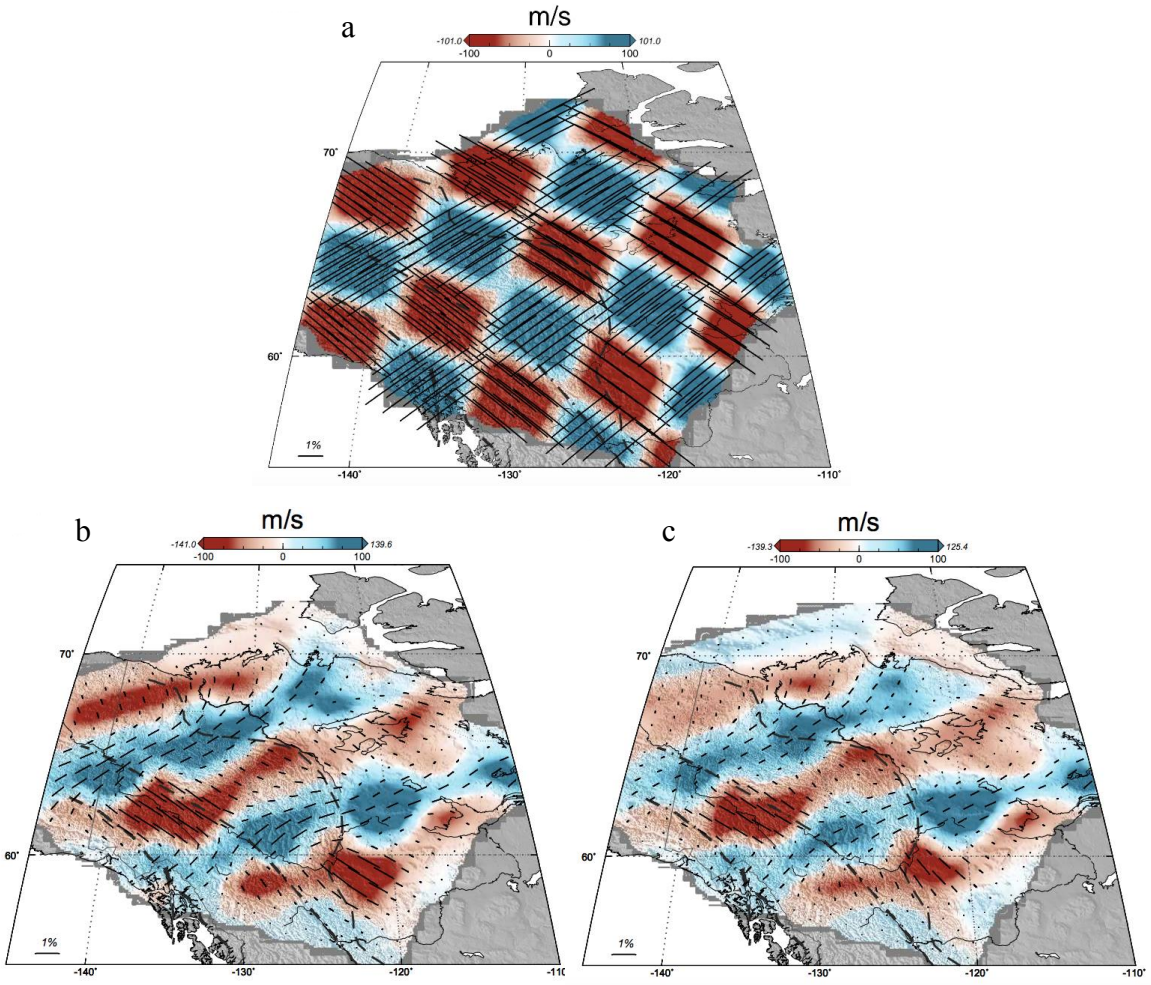

Figure 3.5: Results of checkerboard test. (a) Synthetic input data where the red squares represent negative velocity anomalies and the blue squares represent positive velocity anomalies. Anisotropy is represented by alternating black stick orientations of plus and minus 45°. (b) Result of inversion using path coverage at 15 s. (c) Result of inversion using path coverage at 40 s.

The path sampling observed at a period of 15 s and 40 s was used to recover the input

model for the ambient noise and teleseismic data respectively. The isotropic resolution test shows good resolution of boundaries trending in an east-west direction whereas those trending in a north-south direction experience eastward smearing. This is a result of the dominant west-east path direction within our data due to the preferential nature of noise production and earthquake locations. Outside of the Cordillera, particularly into the Canadian Shield, resolution is poor due to a striking decrease in path coverage. Overall, we estimate that the model can resolve structures of 150 km in size within the Cordillera and 300 km within the Shield. Anisotropic resolution results show similar patterns. Fast axis orientations show good recovery within the central Cordillera but the resolution deteriorates within the surrounding regions. Based on these results, interpretation of small-scale structure (~150 km) is limited to the Cordillera, and only large-scale structure is interpreted within the Shield.

3.4 Phase velocity maps

Isotropic velocity anomalies are plotted as the perturbation from the mean velocity over the entire region at each selected period. Figure 3.6 shows the resulting phase velocity maps at 8 s, 15 s, 25 s, 40 s, 60 s, and 80 s. The approximate corresponding depth ranges are indicated by the sensitivity kernels in Figure 3.7.

At 8-25 s, corresponding with upper to lower crustal depths, we observe a transition from high velocities to low velocities across the Deformation Front, with higher velocities in the Shield and lower velocities in the Cordillera. Conversely, we observe a transition from low to high velocities across the Tintina Fault further to the west. A low velocity anomaly is observed southwest of the Denali Fault at periods of 8 to 25 s and the intensity and scale of this anomaly increases with increasing period. At 8 s a northeast-southwest trending high velocity anomaly is observed within the Mackenzie Mountains that extends from the

Deformation Front in the east to the Tintina Fault in the west. This is in contrast to the strong low velocity anomalies that are observed elsewhere throughout the Mackenzie Mountains. At longer periods (15-25 s) this anomaly is no longer observed. At periods of 8-15 s we also see the small-scale extension of low velocities east of the Deformation Front within the Richardson Mountains. At 25 s this observation is reversed, and we begin to see the extension of high velocities further west into the Cordillera at those high latitudes. At 15 s, as low velocities begin to dominate throughout the Cordillera, small-scale structure is observed. High velocity anomalies are observed within the region between the Tintina and Denali faults and the eastern extent of those anomalies corresponds with the location of the Tintina Fault.

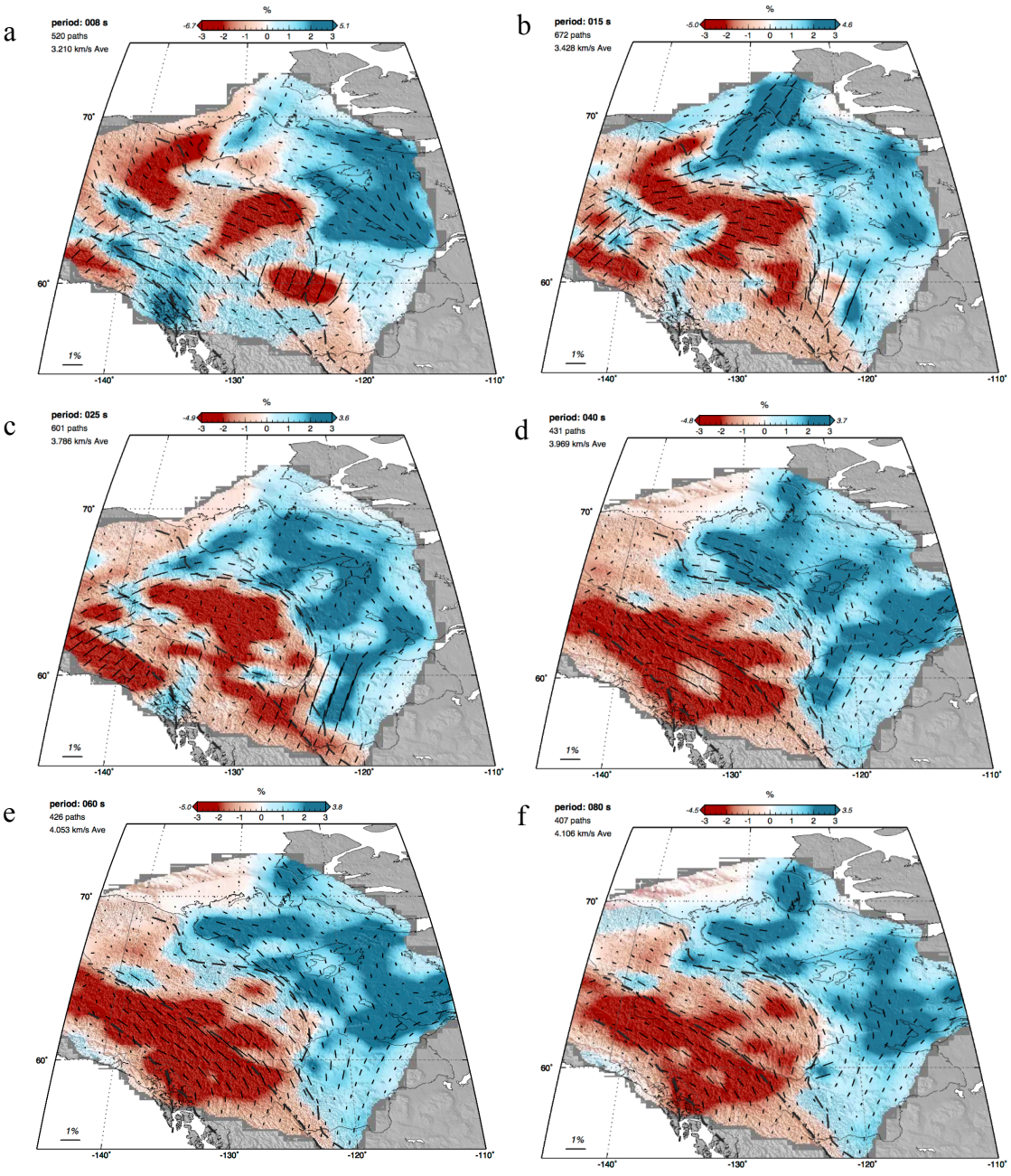

Figure 3.6: Ambient noise (a, b, c) and teleseismic (d, e, f) anisotropic phase velocity maps computed at 8 s (a), 15 s (b), 25 s (c), 40 s (d), 60 s (e), and 80 s (f). Phase velocities are plotted with respect to each panel average (indicated at top left), with the scale bar denoting the difference in percent. The number of inter-station paths contributing data to each period are also indicated top left. Thin black sticks represent the orientation of the fast axis of 2Ψ anisotropy.

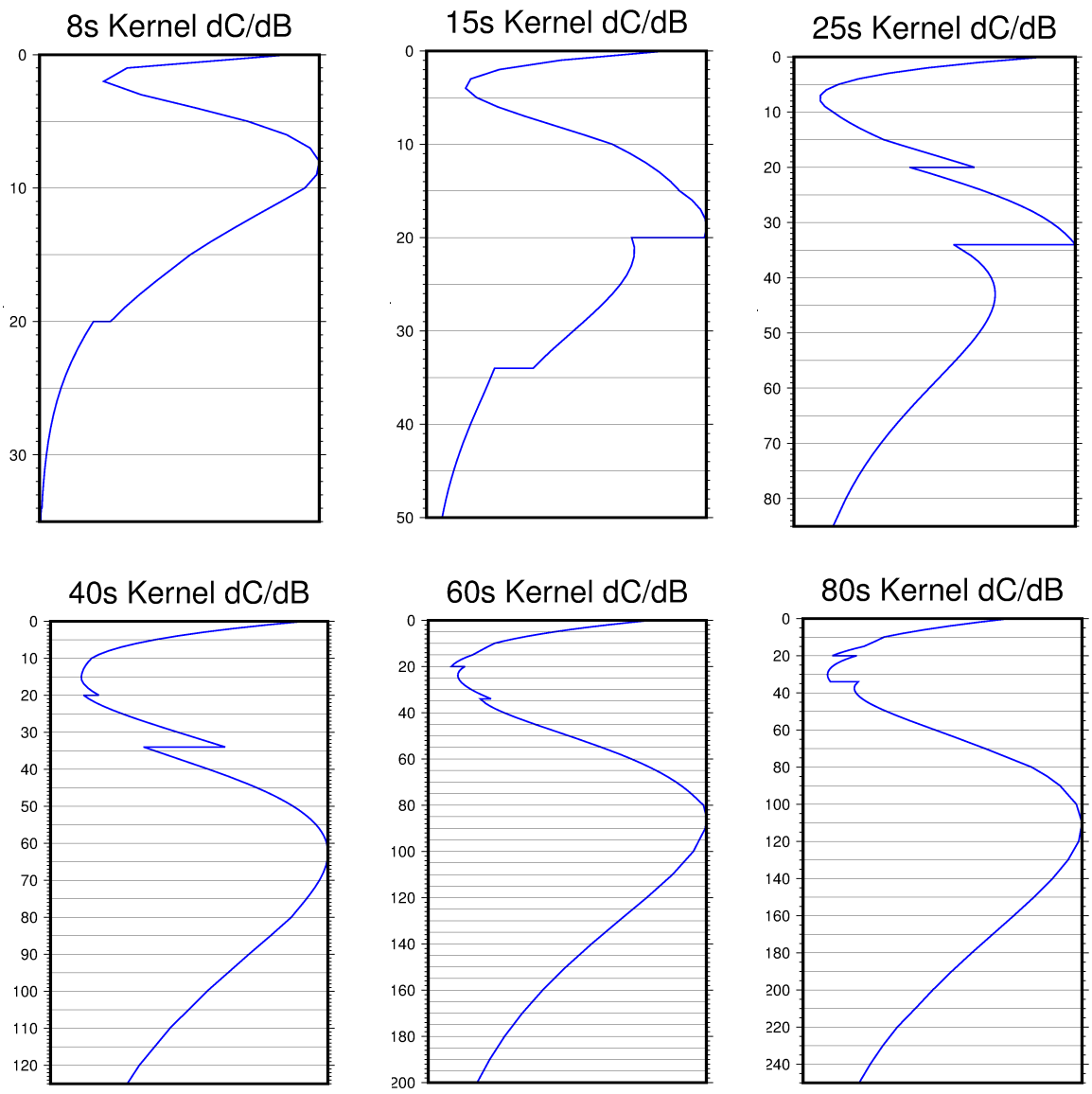

Figure 3.7: Phase-velocity depth sensitivity for each of the periods imaged, calculated for the AK135 reference model (Kennett *et al*., 1995). Sensitivity amplitudes in each panel are scaled independently to their maximum value (i.e., peak amplitude at 15 s is ~4.5 times higher than at 80 s). Complexity at shallow depths results from crustal layering and the Moho in the reference model.

At periods >40 s, corresponding to upper mantle depths, we again see a transition from high velocities in the Shield to lower velocities in the Cordillera. The greatest intensity of low velocities is observed southwest of the Tintina Fault. At longer periods, the transition between

the high velocity and low velocity regions is less well defined along the Deformation Front. Further north we see the extension of high velocities westward past the Deformation Front and within the Cordillera. In this region we also observe a high velocity anomaly at the Canada-US border just north of the Tintina Fault, which is fairly consistent from 40-80 s. Beginning at 40 s, the extension of high velocities west of the Deformation Front is observed further south within the Mackenzie Mountains. This is observed until 80 s, where there is a return to lower velocities.

3.5 Anisotropy

Based on the results of the resolution test, we focus our interpretation of anisotropy to within the central portion of the Cordillera. Results of seismic anisotropy are generally consistent for periods of 8-15 s where the general alignment of the fast axis is with the major faults in the region, specifically the Tintina Fault in the central Cordillera. To the west there is a persistent southwest-northeast alignment of the fast axis around the Yukon-Alaska border, south of the Tintina Fault; however, this pattern may be due to biased path coverage and is poorly resolved. Further east, at the transition from the Cordillera to the Shield, the orientation of the fast axis changes from trending roughly north-south at the Yukon-BC border, to trending northwest-southeast in the Mackenzie Mountains. A rotation of the fast-axis is observed again further north within the Richardson Mountains where the orientation of the fast axis returns to a north-south direction. This change in orientation from northern to southern latitudes reflects the changing orientation of the Deformation Front. At 25 s we see an increase in heterogeneity of fast-axis orientation throughout the Cordillera. The orientation of the fast axis is no longer aligned with the major fault systems and reflects smaller scale structure. At 40-80 s the fast axis orientation remains consistent throughout the Cordillera, again aligning with the Tintina

Fault.

3.6 1-D velocity profiles

Three inversions were carried out for the regions of interest described in section 3.1: southwest of the Tintina Fault (Group 1), the Mackenzie Mountains (Group 2), and east of the Deformation Front (Group 3). The 1-D inversions were produced using two separate background models: one for the two regions located within the Cordillera (Groups 1 and 2) and another for the region east of the Deformation Front (Group 3). The two background models are constructed based on a combination of the global crustal reference model Crust2 (Bassin *et al.,* 2002), AK135, and the sediment thickness map (Mooney & Kaban, 2010). These models were then adapted for the specific regions through alteration of the thickness of the three crustal layers as well as Moho depth. We used a Moho depth estimate of 32.5 km for the Cordillera, and 39 km for the Shield based on previous studies (e.g., Kao *et al*., 2013).

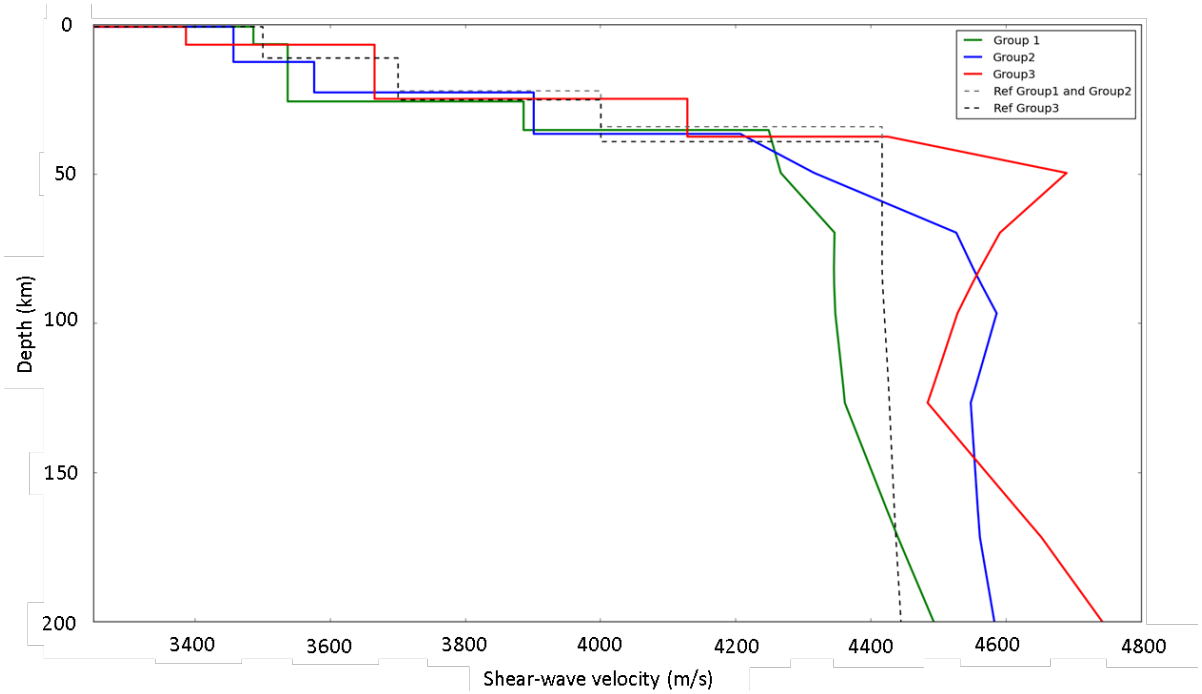

Figure 3.8: Result of 1D inversion plotted for the region west of the Tintina fault (green), the Mackenzie Mountain region (blue), and the shield (red). Background models used for each group are represented by the grey (Groups 1 and 2) and black (Group 3) dashed lines.

Figure 3.8 shows the results of the inversion for the three groups as well as the background models. We report results of absolute shear wave velocities. Based on the three-layer crustal model, the transition from the upper to mid-crustal layer occurs at approximately 6.4 km, 12.31 km, and 6.5 km for Group 1, 2 and 3, respectively. The lowest velocities at those shallow depths (3.4 km/s) are found within the Canadian Shield, although our data set may be only weakly sensitive to shallow structure. The transition from upper to mid-crustal depths sees an increase in velocity from ~3.4 to 3.65 km/s within the Shield, with higher velocities observed within the Shield in comparison to the Cordillera. The Mackenzie Mountains region sees a more significant increase in velocity (3.46 km/s to 3.58 km/s) in comparison to the region west of the Tintina fault (3.49 km/s to 3.54 km/s) resulting in faster velocities now observed within the Mackenzie Mountains region.

The transition from middle to lower crust occurs at approximately 26 km, 23 km, and 25 km for Group 1, 2 and 3, respectively. We continue to observe high velocities in the lower crust within the Shield (~4.1 km/s) in comparison to the Cordillera (~3.9 km/s). Similar velocities are observed within the regions east and west of the Tintina Fault. Moho depths are 35 km for the region west of the Tintina Fault, 36 km for the Mackenzie Mountains region, and 37 km for the Shield. At approximate lithospheric mantle depths (<100 km), general observations show high velocities within the Shield, in comparison to the Cordillera with the slowest velocities observed west of the Tintina Fault. Seismic velocities beneath the Mackenzie Mountains region progressively increase from 4.2 km/s at the Moho to a maximum of ~4.6 km/s at a depth of ~100 km. At that depth the difference between west and east Cordillera (Group 1 and 2) reaches ~0.3 km/s. Results for the Shield region (Group 3) show a large velocity contrast at the Moho with lithospheric mantle velocities reaching a maximum of 4.7 km/s at 50 km depth, followed by a decrease to a minimum of 4.45 km/s at ~120 km.

The large decrease then increase in shear-wave velocity as a function of depth within the Shield at depths of 80—200 km requires further testing.

4. Discussion

4.1 Isotropic Crust and Mantle Structure

At crustal depths seismic velocity is mainly sensitive to the rock composition, and to a lesser extent temperature. The Canadian Shield is characterized by high phase velocity anomalies, reflecting the igneous and metamorphic rocks, which comprise most of the crust. Large low phase velocity anomalies observed within the Cordillera at short periods (shallow depths) east of the Tintina Fault can be correlated with the location of the Cambrian sedimentary rocks of the Selwyn Basin formed at the ancestral passive margin of North America. The sharp transition from low velocities to high velocities westward across the Tintina Fault at upper to mid-crustal depths could reflect the accumulated strike-slip motion of the fault that has transported material of the Intermontane Belt ~450 km from its original location (Hayward, 2015), which now juxtaposes material with different composition and physical properties on either side of the fault. The low velocity signature is associated with the sedimentary rocks of the Selwyn basin whereas the high velocity signature is associated with the crystalline mafic rocks of the Intermontane Belt.

At periods of 15-25 s, low shear-wave velocities throughout the Cordillera possibly reflect the sedimentary rocks deposited along the ancient passive margin of North America that have been deformed to form the Cordillera. The low-velocity, deep crustal layer observed throughout the Cordillera may support the existence of a detachment within the crust, with the detachment separating the rigid upper crust from the weak shear-zone within the lower crust. This interpretation is consistent with previous studies that have suggested the existence of continuous Proterozoic metasedimentary strata within the lower portion of the cordilleran crust (Snyder *et al.*, 2002). In this case, the accreted terranes that are exposed at the surface are thin slices that have been thrust upon the sedimentary rocks. This implies that the western

extent of North America was established prior to major terrane accretion in the Devonian, and that the large crustal faults did not penetrate the entire crust.

Other small-scale features of interest include the northeast trending high velocity anomaly within the Mackenzie Mountains at periods of 8-15 s, which roughly coincides with the location of the Liard Transfer Zone, a northeast trending lineament which is a signature of an ancient transfer fault associated with asymmetric passive margin structures within the region (Cecile *et al*., 1997; Hayward, 2015). In addition, the low velocity anomaly observed west of the Denali Fault is consistent with previous tomography studies of the region (e.g. Ward, 2015). We concur with the interpretation proposed by Ward (2015) where a thick, low-density zone beneath the Chugach Mountains, inferred from gravity anomalies modelled by Mankhemthong *et al*. (2013), is attributed to the uplift of the Chugach Mountains through wedge tectonics. The low-density zone is interpreted as accreted sediments, which are reflected in the low velocities at short periods.

Within the mantle, seismic velocities are predominantly sensitive to temperature (with lower sensitivity to composition) where low seismic velocities reflect elevated temperatures and high seismic velocities reflect lower temperatures. We interpret the low velocities at periods of 40-80 s west of the cordilleran Deformation Front as a reflection of widespread elevated temperatures beneath the Cordillera, supporting the thermal isostasy model of the region (Hyndman & Currie, 2011). The increase in intensity of the low velocity anomaly west of the Tintina Fault may imply that temperatures are even greater beneath the western portion of the Cordillera. These elevated temperatures beneath the Cordillera could be related to younger transition from subduction to accretion west of the Tintina Fault. At periods of 40-80 s our phase velocity maps show relatively high velocities extending west of the Deformation Front, which are interpreted as slightly lower upper mantle temperatures. The boundary

between hot and cold upper mantle is approximately coincident with the surface trace of the Tintina Fault, which also marks the crustal boundary between mafic rocks of the Intermontane Belt and the sedimentary strata to the east. These results may imply that upper mantle temperatures are not uniform beneath the Cordillera.

4.2 Cordillera-Craton Boundary

The Cordillera-Craton boundary defines the transition between thick, cool cratonic lithosphere of the Canadian Shield and thin, hot cordilleran lithosphere. The nature of this boundary has implications regarding the origin and evolution of the Cordillera, as well as the deformation occurring within it. The Cordillera-Craton boundary is generally aligned with the Deformation Front at crustal and mantle depths, with a few exceptions (e.g., toward the north and southeast of the Deformation Front). The continuous nature of this transition along the Front implies that physical properties of cordilleran lithosphere are markedly different from those of the Shield, and that lithospheric and upper mantle structures are somewhat coherent from the surface to ~150 km depth. At crustal depths the transition likely reflects the juxtaposition of crystalline rocks of the Shield to folded sedimentary strata associated with former passive margin structures. In the upper mantle, low shear-wave velocities are associated with a hot and thin mantle lithosphere and underlying asthenosphere. However, as mentioned previously, low shear-wave velocities at upper mantle depths within the Cordillera increase toward the east to values approaching those of the Shield, which suggests that the eastern part of the Cordillera may be underlain by colder lithosphere possibly associated with the westward extension of the Shield beneath the Cordillera. Toward the north, the extension of high velocities west of the Deformation Front has been observed in other tomography studies of the region (e.g. Schaeffer & Lebedev, 2014), and has been attributed to the possible

existence of the "Mackenzie Craton," an Archean continental fragment for which there is some geochemical and geophysical evidence but has no surface expression.

The Cordillera-Craton boundary at lithospheric mantle depths (<100 km) may therefore coincide with the Tintina Fault, as opposed to the Deformation Front. This interpretation is consistent with the eastern Cordillera forming the footwall of the former North American passive margin characterized by a low-angle detachment fault overlain by tilted crustal blocks separated by thick sedimentary basins. The lithosphere of this former footwall structure may have remained stable through various episodes of convergence that created the fold and thrust belt within the Mackenzie Mountains.

4.3 Seismic anisotropy

Seismic anisotropy reflects the coherent alignment of rock fabric, which can be used to constrain the specific geologic and/or tectonic processes from which they originate. There are many different sources of anisotropy within the crust. Examples of such sources include layered sedimentary sequences, micro-fractures, and the alignment of major minerals within foliated rocks. Determining the exact cause of anisotropy can be difficult, especially in regions undergoing complex deformation. Known information about the geology of the region can provide constraints on more likely sources of anisotropy. Babuska & Cara (1991) propose that the cause of anisotropy can change as a function of depth within the crust. They suggest that anisotropy is associated with pervasive fracturing and major stresses within the upper crust, while mineral alignment within foliated and metamorphosed rocks is more commonly observed within the lower crust. Within the mantle, anisotropy is generally attributed to the lattice-preferred orientation of olivine crystals, which reflect active or frozen-in mantle flow.

Within the cordilleran crust, one possible source of anisotropy is the fabric originating

from the assemblage of northwest-southeast trending terranes as described by Rasendra *et al*. (2013). In this case, the fast axis represents frozen-in tectonic fabrics associated with the accretion of terranes throughout the Paleozoic and Mesozoic. Another possible explanation proposed by Rasendra *et al*. (2013) for fast-axis orientations near the Denali Fault is based on continuous long-term shearing along a fault. This interpretation is consistent with our results further east around the Tintina Fault where we also observe fault-parallel fast axis orientations. In both cases fault-parallel fast axis orientations are observed both within the mid-crust and upper mantle. The upper mantle anisotropy can be ascribed to the lattice-preferred orientation of olivine crystals within the mantle penetrating shear zone (Audet *et al.*, 2016).

The consistency of anisotropy throughout the upper-to-mid crust (periods of 8-15 s) implies little variation in rock fabric at these depths. This changes with increasing depth, where an increase in heterogeneity of fast-axis orientation at lower crustal depths is observed. This suggests that the orientation and magnitude of tectonic stresses and/or the rock rheological response to those stresses within the region may vary from those at shallower depths. The orogenic float model postulates the existence of a weak detachment (shear) zone within the lower crust (Mazzotti & Hyndman, 2002). The heterogeneity of the seismic anisotropy at these inferred depths does not reflect the existence of a large-scale uniformly weak shear zone, and therefore may imply the deformation occurring within the lower crust is more complex. However, our seismic anisotropy data set may not be sufficient to rule out this hypothesis.

Within the mantle, fault-parallel fast axis orientations reflect coherency between the crust and mantle. The consistency of the fast axis orientation observed throughout the Cordillera and at different depths implies large-scale, coherently deforming lithosphere and underlying asthenosphere. Elevated temperatures beneath the Cordillera are believed to be the result of rapid small-scale and vigorous convection due to an increase in fluid content as a

result of former subduction. Our results show no evidence of small-scale convection in the sub-lithospheric mantle. Rather, the coherent fabric may reflect long-term, large-scale mantle flow.

5. Conclusion

In this thesis we conduct a high resolution Rayleigh wave tomography study of northwestern Canada. We incorporate both ambient noise and teleseismic earthquake data to construct phase velocity maps at periods sensitive to upper crust to sub-lithospheric mantle depths. In total we processed 453 teleseismic and 696 ambient noise phase velocity dispersion curves, a substantial amount for a region of this size.

Our results show strong correlation between both isotropic and anisotropic velocities with major tectonic structures within northwestern Canada. At crustal depths high phase velocities within the shield reflect igneous and metamorphic composition of the rocks within the craton. Low velocities observed within the Mackenzie Mountains reflect the sedimentary rocks of the Selwyn Basin, and high velocities west of the Tintina Fault correspond with the accreted terranes of the Intermontane Belt which have been mobilized along the fault. The transition to low velocities throughout the Cordillera at greater crustal depths provides evidence for the existence of Proterozoic metasedimentary strata which underlays the majority of the Cordillera. Within the mantle, low velocities observed within the Cordillera in comparison with those observed within the shield supports the thermal isostasy model for the region. Anisotropic fast-axis orientations within the upper crust and mantle run parallel to the major faults within the region reflecting the existence of a predominantly fault-parallel shear zone that extends to lithospheric mantle depths. 1D inversion results show low velocities throughout the lower crust within the Cordillera. This is consistent with the existence of a weak layer within the lower crust, as postulated by the orogenic float model, however the heterogeneous nature of anisotropic fast-axis orientations within the lower crust contradicts the presence of a uniformly shearing layer, implying deformation may be more complex within the lower crust.

Limitations of our results include station coverage within the Cordillera and surrounding regions. This limits resolution, specifically within regions outside of the Cordillera where seismograph stations are sparsely distributed. Further limitations include the lack of incorporation of Love wave data. As Love wave particle motion is contained within the horizontal plane, using them in combination with Rayleigh waves provides additional information about radial anisotropy, as opposed to azimuthal anisotropy measured from each individually. This can provide complementary information about vertical flow and deformation within the crust and mantle, such as the potential signature of extinct subduction zones associated with the assembly of the Cordilleran terranes.

Future considerations for furthering our understanding of cordilleran deformation within northwestern Canada include improving model resolution through the addition of seismograph stations within and around the Cordillera. With the continued installation of the TA network as well as the soon to be installed Mackenzie Array, station coverage within the region will improve substantially. This will improve our ability to observe smaller scale features as well as improve confidence in the location of major tectonic boundaries. Finally, completing a full 3-D inversion of the region using the set of phase velocity maps generated in this study will provide a more complete picture of the shear velocity structure within the northern Canadian Cordillera. This allows one to convert seismic wave velocity into specific properties including composition and temperature providing further crucial constraints on the structure and dynamics of this complex region.

References

Agius, M.R. & Lebedev, S. 2013. Tibetan and Indian lithospheres in the upper mantle beneath Tibet: Evidence from broadband surface-wave dispersion. Geochemistry Geophysics Geosystems. V.14, I. 10, pg. 4260-4281.

Agius, M.R. & Lebedev, S. 2014. Shear-velocity structure, radial anisotropy and dynamics of the Tibetan crust. Geophsical Journal International. V. 199, I. 3, pg. 1395-1415.

Audet, P., Jellinek, A.M., Uno, H. 2007. Mechanical controls on the deformation of continents at convergent margins. Earth and Planetary Science Letters. V. 264, I. 1-2. pg. 151-166.

Audet, P., Sole, C., Schaeffer, A.J. 2016. Control of lithospheric inheritance on neotectonic deformation in Northwestern Canada. Geology, in press.

Babuska, V. & Cara, M. 1991. Seismic Anisotropy in the Earth, Kluwer Acad., Boston, Mass.

Bassin, C., Laske, G., Masters, G. 2000. The current limits of resolution for surface wave tomography in North America. EOS, V. 81, F897.

Bensen, G. D., Ritzwoller, M. H., Barmin, M. P., Levshin, A. L., Lin, F., Moschetii, M. P., Shapiro, N. M., Yang, Y. 2007. Processing seismic ambient noise data to obtain reliable surface wave dispersion measurements. Geophysical Journal International. V. 169, I. 3, pg. 1239-1260.

Bedle, H. & van der Lee, S. 2009. S velocity variations beneath North America. Journal of Geophysical Research-Solid Earth. V. 114, Article Number: B07308.

Campillo, M., Paul, A. 2003. Long-Range Correlations in the Diffuse Seismic Coda. Science. V. 299, I. 5606, pg. 547-549.

Cassidy, J.F., Rogers, G.C., Ristau, J. 2005. Seismicity in the vicinity of the SNORCLE corridors of the northern Canadian Cordillera. Canadian Journal of Earth Sciences. V. 42, I. 6, pg. 1137-1148.

Cecile, M.P., Morrow, D.W., Williams, G.K. 1997. Early Paleozoic (Cambrian to Early Devonian) tectonic framework, Canadian Cordillera. Bulletin of Canadian Petroleum Geology. V. 45, I. 1, pg. 54-74.

Clowes, R.M., Zelt, C.A., Amor, J.R., and Ellis, R.M. 1995. Lithospheric structure in the southern Canadian Cordillera from a network of seismic refraction lines: Canadian Journal of Earth Sciences, v. 32, I. 10, p. 1485-1513.

Cook, F.A., Clowes, R.M., Snyder, D.B., et al. 2004. Precambrian crust beneath the Mesozoic northern Canadian Cordillera discovered by Lithoprobe seismic reflection profiling. Tectonics. V. 23, I. 2, Article Number: TC2010.

Courtier, A.M., Gaherty, J.B., Revenaugh, J., Bostock, M.G., Garnero, E.J. 2010. Seismic anisotropy associated with continental lithosphere accretion beneath the CANOE array, northwestern Canada. Geology. V. 38, I. 10, pg. 887-890.

Currie, C.A., and Hyndman, R.D., 2006, The thermal structure of subduction zone backarcs: Journal of Geophysical Research. V. 111, I. B8, Article Number: B08404.

Dalton, C.A., Gaherty, J.B. 2013. Seismic anisotropy in the continental crust of northwestern Canada. Geophysical Journal International. V. 193, I. 1, pg. 338-348.

Dalton, C.A., Gaherty, J.B., Courtier, A.M. 2011. Crustal Vs structure in northwestern Canada: Imaging the Cordillera-craton transition with ambient noise tomography. Journal of Geophysical Research. V. 116, Article Number: B12315.

Darbyshire, F., Eaton, D. 2010. The lithospheric root beneath Hudson Bay, Canada from Rayleigh wave dispersion: No clear seismological distinction between Archean and Proterozoic mantle. Lithos. V. 120, I. 1-2, pg. 144-159.

Darbyshire, F. & Lebedev, S. 2009. Rayleigh wave- phase-velocity heterogeneity and multilayered azimuthal anisotropy of the Superior Craton, Ontario. Geophysical Journal International. V. 176, I. 1, pg. 215-234.

Deschamps, F., Lebedev, S., Meier, T., Trampert, J. 2008. Azimuthal anisotropy of Rayleigh-wave phase velocities in the east-central United States. Geophysical Journal International. V. 173, I. 3, pg. 827-843.

Doser, D.I., Lomas, R. 2000. The transition from strike-slip to oblique subduction in southeastern Alaska from seismological studies. Tectonophysics. V. 316, I. 1-2, pg. 45-65

Frederiksen, A.W., Bostock, M.G., Cassidy, J.F. 2001. S-wave velocity structure of the Canadian upper mantle. Physics of the Earth and Planetary Interiors. V. 124, I. 3-4, pg. 175-191.

Yuan, H., Romanowicz, B., Fischer, K.M., Abt, D. 2011. 3-D shear wave radially and azimuthally anisotropic velocity model of the North American upper mantle. Geophysical Journal International. V. 184. I. 3, pg. 1237-1260.

Hansen, P.C., 1998. Rank-deficient and discrete ill-posed problems: numerical aspects of linear inversion, SIAM, Philadelphia.

Hayward, N. 2015. Geophysical investigation and reconstruction of the lithospheric structure and its control on geology, structure, and minearlization in the Cordillera of northern Canada and eastern Alaska. Tectonics. V. 34, I. 10, pg. 2165-2189.

Hoffman, P.F. 1988. United Plates of America, The Birth of a Craton: Early Proterozoic Assembly and Growth of Laurentia. Annual Review of Earth and Planetary Sciences. V. 16, pg. 543-603.

Hildebrand, R.S., Hoffman, P.F., Bowring, S.A. 1987. Tectonomagmatic Evolution of the 1.9-GA Great Bear Magmatic Zone, Wopmay Orogen, Northwestern Canada. Journal of Volcanology and Geothermal Research. V. 32, I. 1-3, pg. 99-118.

Hyndman, R.D., Lewis, T.J. 1999. Geophysical consequences of the Cordillera-Craton thermal transition in southwestern Canada. Tectonophysics. V. 306, I. 3-4, pg. 397-422.

Hyndman, R.D., Fluck, P., Mazzotti, S. 2005. Current tectonics of the northern Canadian Cordillera. Canadian Journal of Earth Sciences. V. 42, I. 6, pg. 117-1136.

Hyndman, R.D., Currie, C.A., and Mazzotti, S.P. 2005. Subduction zone backarcs, mobile belts, and orogenic heat: GSA-Today. V. 15, I. 2, pg. 4-10.

Hyndman, R.D., Currie, C.A. 2011 Why is the North American Cordillera High? Hot backarcs, thermal isostasy, and mountain belts. Geology. V.39, I. 8, pg. 783-786.

Johnston, S.T., Mortensen, J.K., Erdmer, P. 1996. Igneous and metaigneous age constraints for the Aishihik metamorphic suite, southwest Yukon. Canadian Journal of Earth Sciences. V. 33, I. 11, pg. 1543-1555.

Kao, H., Behr, Y., Currie, C. A., Hyndman, R., Townend, J., Lin, F., Ritzwoller, M. H., Shan, S., He, J. 2013. Ambient seismic noise tomography of Canada and adjacent regions: Part I. Crustal structures. Journal of Geophysical Research: Solid Earth. V. 118, I. 11, pg. 5865-5887.

Kennett, B. I. N, Engdahl, E.R., & Buland, R. 1995. Constraints on seismic velocities in the Earth from traveltimes. Geophysical Journal International, V. 122, I. 1, pg. 108-124.

Lebedev, S., Boonen, J., Trampert, J. 2008. Seismic structure of Precambrian lithosphere: new constraints from broad band surface-wave dispersion. Lithos. V. 109, I. 1-2, pg. 96-111

Lebedev, S., Adam, J.M., Meier, T. 2013. Mapping the Moho with seismic surface waves: A review, resolution analysis, and recommended inversion strategies. Tectonophysics. V. 609, Special Issue: SI, pg. 377-394

Leonard, L.J., Hyndman, R.D., Mazzotti, S. 2007. Current deformation in the northern Canadian Cordillera inferred from GPS measurements. Journal of Geophysical Research-Solid Earth. V. 112, I. B11, Article Number: B11401.

Leonard, L., Mazzotti, S., Hydnamn, R.D. 2008. Deformation rates estimated from earthquakes in the northern Cordillera of Canada and eastern Alaska. Journal of Geophysical Research-Solid Earth. V. 113, I: B8, Article Number: B08406.

Lewis. T.J., Hyndman, R.D., Fluck, P. 2003. Heat flow, heat generation, and crustal temperatures in the northern Canadian Cordillera: Thermal controls of tectonics. Journal of Geophysical Research-Solid Earth. V. 108, I. B6.

Lobkis, O. I., Weaver, R. L. 2001. On the emergence of the Green's function in the correlation of a diffuse field. Acoustical Society of America. V. 110, I. 6, pg. 3011-3017.

Mankhemthong, N., D. I. Doser, and T. L. Pavlis. 2013. Interpretation of gravity and magnetic data and development of two-dimensional cross-sectional models for the Border Ranges fault system, south-central Alaska. Geosphere. V. 2, I. 2, pg. 242-259.

Mazzotti, S., Hydnman, R.D. 2002. Yakutat collision and strain transfer across the northern Canadian Cordillera. Geology. V. 30, I. 6, pg. 495-498.

Meier, T., Dietrich, K., Stockhert, B., Harjes,H.P. 2004 One-dimensional models of shear wave velocity for the eastern Mediterranean obtained from the inversion of Rayleigh wave phase velocities and tectonic implications. Geophysical Journal International. V. 156, I.1, pg. 45-58.

Mercier J.P., Bostock, M.G., Cassidy, J.F., Dueker, K., Gaherty, J.B., Garnero, E.J., Revenaugh, J., Zandt, G. 2009. Body-wave tomography of western Canada. Tectonophysics. V. 475, I. 3-4, pg 480-492

Monger, J. & Price, R. 2002. The Canadian Cordillera: Geology and Tectonic Evolution. CSEG Recorder.

Mooney, W.D., Kaban, M.K. 2010. The North American upper mantle: Density, composition, and evolution. Journal of Geophysical Research-Solid Earth. V. 115, Article Number: B12424.

Nelson, J. L., M. Colpron. 2007. Tectonics and Metallogeny of the British Columbia, Yukon, and Alaskan Cordillera, 1.8 Ga to the Present. Mineral deposits of Canada: a synthesis of major deposit-types, district metallogeny, the evolution of geological provinces, and exploration methods; by Goodfellow, W D (ed.); Geological Association of Canada, Mineral Deposits Division. Special Publication no. 5, pg. 755-791.

Nelson, J. L., M. Colpron, and S. Israel (2013), The Cordillera of British Columbia, Yukon, and Alaska, in Tectonics, Metallogeny, and Discovery: The North American Cordillera and Similar Accretionary Settings, Soc. Econ. Geol. Spec. Publ. V. 17, pg. 53-109

Nicolson, H., Curtis, A., Baptie, B., Galetti, E. 2009. Seismic Interferometry and ambient noise tomography in the British Isles. Proceedings of the Geologists' Association. V. 123, I. 1, pg. 74-86.

Nishenko, S.P., Jacob, K.H. 1990. Seismic potential of the Queen-Charlotte-Alaska-Aleutian seismic zone. Journal of Geophysical Research-Sold Earth and Planets. V. 95, I. B3, pg. 2511-2532.

Paige, C. & Saunders, M. 1982. LSQR: an algorithm for sparse linear equations and sparse least squares. Trans. Math. Softw. V. 8, I. 1, pg. 43-71.

Perry, H.K.C., Eaton, D.W.S. Forte, A.M., 2002, LITH5.0: a revised crustal model for Canada based on Lithoprobe results: Geophysical Journal International, V. 150, I. 1, pg. 285-294.

Rasendra, N., Bonnin, M., Mazzotti, S., Tiberi, C. 2013. Crustal and Upper-Mantle Anisotropy Related to Fossilized Transpression Fabric along the Denali Fault, Northern Canadian Cordillera. Bulletin of the Seismological Society of America. V. 104, I. 4, pg. 1964-1975.

Schaeffer, A. J., Lebedev, S. 2013. Global shear speed structure of the upper mantle and transition zone. Geophysical Journal International. V. 194, I. 1, pg. 417-449.

Schaeffer, A.J., Lebedev, S. 2014. Imaging the North American continent using waveform inversion of global and USArray data. Earth and Planetary Science Letters. V. 402, Special Issue: SI.

Shapiro, N. M., Campillo, M. 2004. Emergence of broadband Rayleigh waves from correlations of ambient seismic noise. Geophysical Research Letters. V. 31. I. 7, Article Number: L07614.

Smith, M. L. & Dahlen, F. A. 1973. The azimuthal dependence of Love and Rayleigh wave propagation in a slightly anisotropic medium. Journal of Geophysical Research. V. 78, I. 17, pg. 3321-3333.

Snyder, D. B., Clowes, R.M., Cook, F. A., Erdmer, P. Evenchick, C. A., van der Velden, A. J. and Hall, K. W. 2002. Proterozoic prism arrests suspect terranes: Insights into the ancient cordilleran margin from seismic reflection data, GSA Today, V. 12, I. 10, pg. 4–10.

Snyder, D. B., Pilkington M., Clowes, R. M., and Cook, F. A. 2009. The underestimated Proterozoic component of the Canadian Cordillera accretionary margin, in Earth Accretionary Systems in Space and Time, Geol. Soc. Spec. Publ., 318, pg. 257–271.

Ward, K.M. 2015. Ambient noise tomography across the southern Alaskan Cordillera. Geophysical Research Letters. V. 42, I. 42, pg. 3218-3227.